Septins promote F-actin ring formation by crosslinking actin filaments into curved bundles

M. Mavrakis, Y. Azou-Gros, Feng-Ching Tsai, J. Alvarado, A. Bertin, F. Iv, Alla Kress, S. Brasselet, Gijsje H. Koenderink, Thomas Lecuit

Septins promote F-actin ring formation by cross-linking actin filaments into curved bundles

Manos Mavrakis[1]*, Yannick Azou-Gros[1], Feng-Ching Tsai[2,5], José Alvarado[2,5], Aurélie Bertin[3,5], Francois Iv[1], Alla Kress[4], Sophie Brasselet[4], Gijsje H. Koenderink[2] and Thomas Lecuit[1]*

[1] Institut de Biologie du Développement de Marseille, CNRS UMR 7288, Aix-Marseille Université, 13288 Marseille, France.

[2] FOM Institute AMOLF, 1098 XG, Amsterdam, The Netherlands.

[3] Institut Curie, CNRS UMR 168, 75231 Paris, France.

[4] Institut Fresnel, CNRS UMR 7249, Aix-Marseille Université, Ecole Centrale Marseille, 13397 Marseille, France.

[5] These authors contributed equally to this work.

* Correspondence:

manos.mavrakis@univ-amu.fr

thomas.lecuit@univ-amu.fr

Animal cell cytokinesis requires a contractile ring of cross-linked actin filaments and myosin motors. How contractile rings form and are stabilized in dividing cells remains unclear. We address this problem by focusing on septins, highly conserved proteins in eukaryotes whose precise contribution to cytokinesis remains elusive. We use the cleavage of the *Drosophila* embryo as a model system, where contractile actin rings drive constriction of invaginating membranes to produce an epithelium in a manner akin to cell division. In vivo functional studies show that septins are required for generating curved and tightly packed actin filament networks. In vitro reconstitution assays show that septins alone bundle actin filaments into rings, accounting for the defects in actin ring formation in *septin* mutants. The bundling and bending activities are conserved for human septins, and highlight unique functions of septins in the organization of contractile actomyosin rings.

Cross-linked actin filaments and myosin motor proteins form the contractile networks that drive cell and tissue shape changes. The contractile ring is an actomyosin assembly which forms at the cell equator during animal cell cytokinesis and constricts the cell membrane to separate the daughter cells. Despite extensive research on contractile ring components, the mechanisms governing its precise structural organization remain poorly understood [1, 2]. In particular, how actin filaments are bent at the plasma membrane — a requirement that becomes more important as the membrane curvature increases over the course of membrane constriction— is unclear. Myosin-II-mediated contractile forces alone tend to buckle and fragment, rather than bend, actin filaments [3, 4].

Screens for cytokinesis-involved genes have identified a conserved core of ~20 proteins, including septins [5]. Septins self-assemble into heteromeric complexes, which can polymerize into higher-order structures [6], and bind membranes [7, 8], Anillin [9-11] (an actin cross-linker present at the cytokinetic ring in most animal cells) and nonmuscle myosin-II [12, 13] in different organisms. How these interactions are coordinated during cytokinesis is unknown. Septins have been proposed to form a membrane diffusion barrier at the cleavage furrow of dividing animal cells [14], similar to septin-dependent diffusion barriers at the plasma membrane and internal membranes of budding yeast [15], but this hypothesis has not been formally tested during animal cytokinesis. Furthermore, septins are thought to serve as an indirect membrane anchor for the contractile ring by interacting with lipids and Anillin. However, Anillin is targeted to the cleavage furrow independently of septins,

and its PH domain is essential for recruiting septins to the furrow[9, 16, 17]. In cultured cells, septin-dependent membrane anchoring defects occur during abscission[17], questioning whether septins bind furrow membranes directly during the constriction step of cytokinesis. Finally, actin organization is impaired in the absence of septins in cleaving *Drosophila* embryos and interphase human cells [10, 18]. No direct actin-septin interaction was documented but septins were reported to interact with nonmuscle myosin-II in interphase and dividing human cells [12, 13]. As Anillin is nuclear during interphase[11, 19], it remains unclear if septins organize actin based on the availability of interacting partners which themselves bind actin in a cell-cycle dependent manner.

We use the cleavage of the *Drosophila* embryo (Fig. 1a) to elucidate how septins contribute to the organization of contractile actomyosin rings. During *Drosophila* embryonic cleavage, called cellularization, membranes invaginate between nuclei to convert the syncytial embryo into thousands of polarized epithelial cells in a process akin to cytokinesis [20, 21]. We combine *in vivo* functional studies and ultrastructural approaches in the *Drosophila* embryo with *in vitro* reconstitution of actin filaments with purified septins to elucidate the molecular interplay between actin and septins.

RESULTS

Defects in Actomyosin assembly kinetics in *septin* mutants

Cellularization involves membrane invagination perpendicular to the embryo surface followed by constriction of the membrane front in a plane parallel to

the embryo surface. The membrane front (called furrow canal, FC) is analogous to the cytokinetic ring, containing actin filaments (F-actin), nonmuscle Myosin-II (hereafter Myo-II), Anillin, and septins (inferred by the localization of the septins, Pnut/hSep7, DSep1 and DSep2). This contractile machinery assembles and is maintained at the FC throughout cellularization (Fig. 1b,c and Supplementary Fig. 1a,b), and is thought to stabilize the tip of the invaginating membranes and drive membrane constriction [9, 21, 22].

We compared membrane invagination in wild type and in *pnut* null mutants (hereafter called *septin* mutants) where DSep1 [18, 23] and thus septin hexamers [24] are absent (Fig. 1d and Supplementary Fig. 1a,b,e). We measured membrane progression in embryos expressing a functional GFP fusion of myosin regulatory light chain (MRLC::GFP) [25] (Fig. 1e and Supplementary Video 1). Invagination in *septin* mutants proceeded in a slow and fast phase, as for wild type embryos [26] (Fig. 1f,g). Whereas membranes invaginated at the same rate during the slow phase (0.14 ± 0.02 μm/min and 0.12 ± 0.02 μm/min for wild type and mutant, respectively), membranes in mutants invaginated significantly more slowly during the fast phase (0.62 ± 0.05 μm/min vs. 0.90 ± 0.09 μm/min for the wild-type, $P = 0.0022$). As a result, mutants took significantly longer to complete cellularization (84 ± 4 min vs. 76 ± 3 min for wild type, $P = 0.0087$).

To test if the slower invagination rate in *septin* mutants reflected defects in the actomyosin ring, we quantified the levels of myo-II and F-actin. Myo-II levels at the FC increased 3-fold during the slow phase in wild-type reaching a maximum of 3.5-fold increase 10 min into the fast phase (Fig. 1h). In *septin*

mutants, Myo-II localized to FCs (Fig. 1e and Supplementary Fig. 1e) but only accumulated 2.5 fold (Fig. 1h). We quantified F-actin by expressing the actin-binding calponin-homology domain of utrophin (UtrCHD::GFP) (Fig. 1i and Supplementary Fig. 1f). Similar to Myo-II, F-actin localized to FCs in *septin* mutants (Supplementary Fig. 1f). Mutant and wild type embryos showed the same maximum increase in F-actin levels (1.5-fold), but with a delay in *septin* mutants (Fig. 1i).

The defects in the kinetics of actin and Myo-II recruitment at the FC suggest a septin requirement for proper actomyosin ring assembly. Given that septins organize membrane diffusion barriers [15], we tested if the FC in *septin* mutants was specified as a distinct membrane domain. In wild-type, the membranes at the FC have a teardrop shape (Fig. 1a-c), and lateral membrane markers are segregated from FC membrane markers (Supplementary Fig. 1a, c, d, wild type panels). This shape was lost in mutants, and the membranes at the FC appeared flatter and deformed (arrowheads in Supplementary Fig. 1c and 4b). However, FC membrane proteins still localized specifically to the FC (Supplementary Fig. 1c), and grazing sections showed that FC markers segregated from lateral membrane proteins (Supplementary Fig. 1d), indicating that a septin-dependent diffusion barrier is not involved in the polarized segregation of several cortical proteins in the FC.

Septins are required for actin filament circularization and compaction

F-actin defects in fixed *septin* mutant embryos were previously reported during the fast phase of cellularization, but their origin was not identified [18].

Our immunostainings revealed F-actin organization defects already during the slow phase. F-actin formed polygonal arrays and loosely organized bundle-like structures, and became progressively more diffuse at the FC (Supplementary Fig. 2). To test whether these defects reflect the destabilization of transiently-formed rings or a complete failure to circularize actin, we performed time-lapse imaging of F-actin at the FC. In wild type, F-actin progressively organized into rings over the course of the slow phase (Fig. 2a). F-actin in *septin* mutants concentrated along the sides of polygon-shaped arrays from the onset of cellularization (Fig. 2b). In wild type, Myo-II organized in foci which progressively redistributed into continuous ring-like structures during the slow phase (Fig. 2c, Supplementary Video 2), whereas in *septin* mutants Myo-II foci clustered unevenly and redistributed over time in polygonal arrays as F-actin (Fig. 2d, Supplementary Video 2). Myo-II and F-actin co-localized in bar-like structures at the FC throughout cellularization (Fig. 2k, left and middle panels).

The aberrant F-actin and Myo-II organization suggests that contractile forces are unable to constrict the membrane front in *septin* mutants. We performed two-photon imaging to measure FC constriction kinetics (Fig. 2e,f), and tracked FC perimeter and circularity during constriction (Supplementary Fig. 2e,f). In wild type, FCs constricted slowly during the slow phase, and switched to a rapid constriction phase upon entry into the fast phase, which lasted until the end of cellularization (Supplementary Fig. 2e). The perimeter decreased ~ 2.5-fold during the rapid constriction phase. F-actin and Myo-II accumulated less than expected based on this degree of constriction, indicating that ring

constriction is coupled with progressive ring disassembly, consistent with observations in *C. elegans* embryos [27]. FCs in *septin* mutants constricted less efficiently (Fig. 2g) and their circularity decreased over time, in contrast to wild type (Fig. 2i). The distribution of FC perimeters and circularities at any time point was significantly broader for *septin* mutants (Fig. 2h,j, $P < 10^{-4}$), reflecting the spatially irregular constriction behavior across the tissue in the absence of septins.

Given the reduced Myo-II levels at FCs in *septin* mutants, we tested if a deficit in contractility alone could account for the failure of FCs to circularize. As RhoGEF2 is the major contractility regulator at the FC [28], we examined F-actin ring formation and constriction in *DRhoGEF2* null embryos where septins are present (Fig. 3b and [28]) but Myo-II is severely reduced (Fig. 3c and [29]). Consistent with previous reports [28-30], FCs in *DRhoGEF2* mutants failed to constrict (Fig. 3a). However, in sharp contrast to *septin* mutants, F-actin rings formed normally and never organized in polygonal arrays. F-actin rings were frequently multinucleated in *DRhoGEF2* mutants, in contrast to both wild-type and *septin* mutants. Thus, Myo-II reduction alone and a consequent deficit in contractility cannot explain the actin ring defects in *septin* mutants. To probe Myo-II activity, we stained embryos with antibodies against total MRLC, monophosphorylated MRLC (Ser21) and diphosphorylated MRLC (Thr20Ser21) (Fig. 3d). Myo-II at the FC was monophosphorylated in wild-type, consistent with a previous report[31], and no signal was detected for diphosphorylated MRLC. *septin* mutants showed a similar pattern (Fig. 3d). Immunoblots of monophosphorylated MRLC showed no difference between

wild-type and *septin* mutants (Fig. 3e). Thus, Myo-II activity is not misregulated in *septin* mutants.

Anillin, which binds and recruits septins to the FC[9], was present at the FC throughout cellularization in *septin* mutants, consistent with prior observations [18], colocalizing with F-actin and Myo-II along the sides of polygonal arrays (Fig. 2k,l ; compare with wild-type in Fig. 1b). Anillin point mutations that compromise septin binding to Anillin and thus to the FC (but not Anillin protein expression or stability per se) were reported to lead to similar actin organization defects as the ones observed in *septin* mutants [9]. Thus the failure to circularize and compact actin filaments in *septin* mutants is due to the absence of septins, rather than Anillin.

F-Actin is loosely packed and disorganized in *septin* mutants

Given the irregular actomyosin distribution at the FCs of *septin* mutants, we examined its ultrastructure by electron microscopy (EM). The organization of the F-actin at the FC is unknown. Sections parallel to the lateral membranes (Fig. 4a, sections *b*, *d*), and parallel to the bases of FCs (Fig. 4a, sections *c*, *e*) in wild type embryos revealed a curved electron-dense coat lining the sides and the base of the FCs (Fig. 4b,c and Supplementary Fig. 3b,d), consistent with the dense actin cytoskeleton observed by light microscopy. In *septin* mutants, an electron-dense coat lining the FC membrane (Fig. 4b and Supplementary Fig. 3b) was detected consistent with light microscopy, however, this was twice as thick in *septin* mutants (112 ± 35 nm vs. 60 ± 20 nm, $P < 2.0\times10^{-6}$, Fig. 4f). To test if this coat thickening was due to a looser

packing of the actin cytoskeleton or to the more material accumulation, we compared coat intensity relative to the adjacent cytoplasm (Supplementary Fig. 3a). Coats in mutant embryos were significantly less dense than in wild type (Fig. 4g, $P = 1.0\times10^{-5}$), indicating a looser packing.

Grazing sections at FC sides (Fig. 4a, section *d*) and bases (Fig. 4a, section *e*) in wild type embryos revealed F-actin bundles parallel to the membrane (Fig. 4d,e and Supplementary Fig. 3c,e), in regions lacking ribosomes. This bundled organization was not observed in *septin* mutants (Supplementary Fig. 3c).

F-Actin molecular orientational order is decreased in *septin* mutants

To probe the degree of orientational order of actin filaments, we imaged Alexa Fluor-488 phalloidin-stained embryos by polarization resolved fluorescence microscopy. Rotating the linear incident polarization in the sample plane leads to a modulation of the fluorescence signal: a strong fluorescence modulation contrast indicates high order (almost parallel dipoles in the focal volume of excitation), whereas low fluorescence modulation contrast reveals disorder (almost isotropic assemblies of dipoles). The maximum fluorescence signal points to the average direction of the dipoles. Analysing this modulation, deduces the molecular orientational order angle ψ (which defines the molecules' angular constraint) and the mean orientation angle ρ (which defines how the molecules are globally oriented in the sample plane) (Fig. 5a)[32].

Polarization resolved fluorescence images showed that the fluorophores had large orientational freedom along the lateral membranes of wild-type and *septin* mutants (Fig. 5b,e, mean ψ= 160°, $P > 0.2$), indicating that cortical actin at the lateral membranes is not ordered. In contrast, an angular constraint of 140° was evident around the circular contour of FCs in wild-type embryos compared to the lateral membrane (Fig. 5c,e, $P = 1.0 \times 10^{-5}$), consistent with tightly packed actin filaments. The orientational order of actin filaments was significantly reduced at the FCs of *septin* mutants, with an aperture angle of 161° (Fig. 5d,e, $P = 1.0 \times 10^{-5}$). Thus, actin filaments are more loosely packed at the FCs of mutant embryos compared to wild type. In wild-type embryos, the mean orientation of actin filaments was azimuthal around the FCs' circular contours (Fig. 5g), thus running parallel to the membranes, consistent with the organization of filaments in grazing sections by EM (Fig. 4d,e). In contrast, actin filaments in *septin* mutants did not always follow the FCs' contours (Fig. 5f,h) and the distribution of ρ angles with respect to the azimuthal direction at given subregions of the contour was broader than in wild-type (Fig. 5i), consistent with the absence of filament organization in *septin* mutants by EM (Supplementary Fig. 3c). For reference, we measured the orientational order of phalloidin-stained stress fibers in COS-7 cells. For these densely packed actin bundles we measured a mean ψ angle of 137° (measured on 12 cells), indicating that F-actin packing in bundles at the FC in wild-type embryos is comparable to the tightly-packed F-actin in stress fibers (Fig. 5j).

Septins directly bind and cross-link actin filaments

Based on the defects in actin filament circularization and packing observed by immunostainings, live imaging, EM and polarization resolved fluorescence imaging, we hypothesize that septins are involved in packing and/or circularizing actin filaments. High-speed F-actin co-sedimentation assays with purified recombinant DSep1-DSep2-Pnut/hSep7 complexes (Fig.6a and Fig. 7c) demonstrated that F-actin-septin binding was saturable with an equilibrium dissociation constant, K_d, of 1.2 ± 0.5 μM (Fig. 6b, 3 independent experiments). Thus, septins bind F-actin with an affinity comparable to actin cross-linkers such as Fascin, Filamin and α-Actinin (K_d in the range of 0.1 to 5 μM). F-actin was also pelleted in the presence of septins by low speed co-sedimentation, demonstrating that septins bundle actin filaments, as single actin filaments are not pelleted at low speed (Fig. 6c and Supplementary Fig. 4a,b).

Septins bundle and bend actin filaments into rings

Imaging of dilute solutions of fluorescently-labeled actin filaments (1 μM) by TIRF microscopy revealed that in the absence of cross-linkers, actin formed isolated filaments (Fig. 6d). In the presence of fly septins (for concentrations > 0.05 μM) actin formed bundles (Fig. 6d) of highly curved geometries, including rings, loops, and lariat-shaped structures, in contrast to the straight F-actin bundles formed in the presence of Fascin (Fig. 6d). Septins decorated bundled F-actin (Fig. 6e), corroborating that fly septins bind F-actin directly. Recombinant human hSep2-hSep6-hSep7 complexes[33] (Supplementary Fig.

5e) behaved as fly septins, generating actin bundles with highly curved geometries at the same concentrations (Fig. 6d).

Given that recombinant purified yeast septins[34, 35] and insect-cell derived human septins[10] are known to form rings at low salt, we wondered whether fly septins at the low salt (50 mM KCl) conditions of our reconstitution assays polymerized into rings, which then template the formation of curved actin bundles. Septins alone did not polymerize when diluted to low salt for septin concentrations < 0.2 μM (Fig. 7b). Time-lapse imaging of polymerizing actin under these conditions showed formation of persisting bends as actin polymerized to form bundles (Fig. 8d and Supplementary Video 3, compare with single actin filaments in Fig. 8e and Supplementary Video 4). Thus, under conditions where septins are not themselves filamentous, they curve and bundle actin filaments during actin polymerization.

To resolve the ultrastructure of septin-actin bundles, we performed EM. Consistent with TIRF microscopy, we detected single filaments for F-actin alone (Fig. 7a). Purified *Drosophila* septins at high salt (300 mM KCl) organized in 4-nm wide by 24-nm long hexameric complexes with septin monomers arranged in a linear manner, consistent with other model systems [36] and biochemical work [24] (Fig. 7c). Consistent with fluorescence microscopy, EM of actin copolymerized with septins revealed curved, looped and splayed filament bundles (Fig. 7d,e). Bundles were decorated with electron-dense material that corresponded to septins, as revealed by nickel-gold decoration (Fig. 7g,h). This protein decoration appeared patchy (Fig. 7g, note the septin hexamers surrounding the actin bundle), and only actin filaments were

detected, distinguishable by their characteristic helical pattern (Fig. 7e). High magnification micrographs revealed fuzzy transverse bands with a periodicity of 37.5 ± 2.9 nm (14 measurements) (Fig. 7f). This value is close to the helical pitch of actin filaments (35.7 nm) [37], consistent with actin filaments being ordered along their long axis. Such periodic transverse bands have been observed for actin cross-linkers such as Fascin and Cortexillin [38, 39].

At concentrations above 0.2 μM, purified septins self-assembled into bundles consistent with previous reports[10, 24, 35, 40, 41]. These bundles were straight, showing only occasionally slight kinks or bends (Fig. 8a,b), consistent with fly embryo-purified septins forming straight bundles[24]. No single septin filaments or bundle rings were detected. When pre-formed fluorescent septin bundles (Fig. 8a) were mixed with G-actin, we observed a co-existence of straight and curved actin bundles. Straight actin bundles correlated with a dense and strong septin signal, whereas curved bundles were decorated with sparser, spottier and dimmer septin signal (Fig. 8c) as that observed for low septin concentrations (Fig. 6e). The stronger septin signal on straight actin bundles was not due to thicker actin bundles, as actin rings with dim and spotty septin signal were thicker than straight actin bundles (see arrowheads in Actin panels and contrast-enhanced septin panels in Fig. 8c). Although we cannot exclude that septins might polymerize following actin binding, based on our observations the septin signal on straight actin bundles likely corresponds to preformed septin bundles, whereas the septin signal on actin rings corresponds to septin hexamers.

DISCUSSION

Our findings demonstrate that septins are required for generating curved and tightly packed actin filament networks at the furrow canal (Fig. 8f). Given that the F-actin bundling and bending activity is conserved for fly and human septins, we predict that septins contribute to the assembly, stabilization and contractility of cytokinetic rings. Septin depletion in dividing cultured cells, where Anillin is localized to the cleavage furrow[16, 42, 43], leads to furrow instability[17, 44, 45] suggesting that the septin F-actin bundling activity could be required for proper cortical tension at the equator or/and the poles, which is in turn critical for the positioning of the cytokinetic ring[46]. Defective formation or stabilization of curved F-actin could further contribute to furrow shape instability. Decreased cytokinetic ring contractility was also recently confirmed in dividing *Drosophila septin* mutant epithelia [47, 48], where Anillin localizes to the cleavage furrow[9, 48].

Septins could also potentially contribute to the shape of furrow canals in actin-independent ways. Recent studies provide compelling evidence that septins regulate the mechanical properties of the cortex in nondividing mammalian cells[45, 49, 50]. Septins were also proposed to provide the cortical rigidity and membrane curvature necessary for rice blast fungal infection[51]. It will be important to test if septins bind membranes at the furrow canal, and how this might synergize with actin cross-linking for cortex organization.

Our findings indicate that the F-actin bending activity of septins requires septin hexamers and not septin filaments, although we cannot exclude that they both function together *in vivo*. Septin post-translational modifications

might also promote septin filament ring formation[34], which might in turn organize F-actin in curved bundles. Actin filaments could also potentially act in septin filament nucleation, even under conditions where septins alone do not form filaments. It will be important to compare the actin remodeling activity of septin hexamers and octamers, given that human septins (unlike *Drosophila* septins[52]) form octamers with hSep9 at the ends[53, 54].

A striking feature of septins is that they bend actin into rings and other highly curved geometries. Actin circularization is energetically unfavorable due to the large bending rigidity of actin filaments [55]. Thus far, stable actin circles have only been reported under strong adhesion mediated by divalent cations [56] or positively-charged lipid monolayers [57]. The adhesion energy mediated by septins appears sufficiently high to overcome the large bending energy associated with such a highly curved geometry. In cells, septin-mediated actin curving may act in synergy with myosin-induced actin filament buckling [3, 4].

Septins could conceivably cross-link F-actin into loose contractile networks in processes that do not involve contractile F-actin rings, depending on the local septin and actin filament concentration and turnover, and septin post-translational modifications. Although no direct actin-septin interaction is known in interphase cells, their interplay has been reported in non-dividing cells[10, 13, 50, 58, 59], despite Anillin's nuclear confinement [11, 19]. Our study suggests that septins, alone or together with myosin-II[12, 13], could contribute to these biological processes through their F-actin bundling activity.

Mammalian septins are known to interact with exocyst components and SNAREs and to regulate membrane fusion (reviewed in[60]). Membrane growth

during cellularization relies on vesicular trafficking (reviewed in[61]), and the exocyst is necessary for this process[62]. As membrane growth is delayed in septin *mutants* (Fig. 1), it will be important to test if septins mediate trafficking events that interplay with actin remodeling at the furrow canal to drive membrane growth[61].

ACKNOWLEDGMENTS

We thank the Lecuit and Lenne groups for discussions and for providing a fruitful environment during the course of this work. We thank Jean-Paul Chauvin, Aïcha Aouane and Fabrice Richard at the IBDM electron microscopy facility for help with embryo processing and image acquisition, Gerard Pehau-Arnaudet at Imagopole (Institut Pasteur) and the electron microscopy facility at Imagif (Gif sur Yvette), Patrick Ferrand, Xiao Wang, Julien Duboisset and Hervé Rigneault (Institut Fresnel) for their contribution in the implementation of polarization resolved fluorescence microscopy, Christophe Romier and Carlos Fernández-Tornero for discussions on septin purification, Flavio Maina for key advise on phosphoprotein Westerns, Marjolein Kuit-Vinkenoog for G-actin purification, and Adam Kamor and Cristel Chandre for Matlab and POV-ray code for drawing furrow canal tori. M.M., Y.A.-G. and F.I. were supported by the ANR Blanc ARCHIPLAST (T.L.), the Fondation pour la Recherche Medicale (équipe labelisée, T.L.), the Association pour la Recherche contre la Cancer (Programme ARC, SL220120605305) and the CNRS. M.M., A.B., F.-C.T., J.A. and G.H.K. were supported by two PHC Van Gogh grants (#25005UA and #28879SJ, ministères des Affaires étrangères et de

l'Enseignement supérieur et de la Recherche), and G.H.K., F.-C.T., J.A. were supported by a VIDI grant from NWO and the Foundation for Fundamental Research on Matter (FOM). A.K. and S.B. were supported by the CNRS, the ANR BLANC grants 150902 (ReceptORIENT) and 18818 (RADORDER) and the region Provence Alpes Côte d'Azur. This work was supported by the national infrastructure France Bio-Imaging and the Nikon Application Center Marseille.

COMPETING FINANCIAL INTERESTS

The authors declare no competing financial interests.

AUTHOR CONTRIBUTIONS

Experiments were conceived and planned by M.M., G.H.K. and T.L. Experiments were performed by M.M., Y.A.-G., F.-C.T., J.A., A.B., F.I. and A.K. Data analysis was performed by M.M., Y.A.-G., A.B., A.K. and S.B. M.M. wrote the first version of the manuscript, and T.L. and G.H.K. contributed to the writing of the final version. F.-C.T., J.A., A.B. and S.B. contributed to the writing of the methods. All authors participated in the discussion of the data and in producing the final version of the manuscript.

REFERENCES

1. Eggert, U.S., Mitchison, T.J. & Field, C.M. Animal cytokinesis: from parts list to mechanisms. *Annual review of biochemistry* **75**, 543-566 (2006).
2. Green, R.A., Paluch, E. & Oegema, K. Cytokinesis in animal cells. *Annual review of cell and developmental biology* **28**, 29-58 (2012).
3. Murrell, M.P. & Gardel, M.L. F-actin buckling coordinates contractility and severing in a biomimetic actomyosin cortex. *Proceedings of the National*

Academy of Sciences of the United States of America **109**, 20820-20825 (2012).
4. Vogel, S.K., Petrasek, Z., Heinemann, F. & Schwille, P. Myosin motors fragment and compact membrane-bound actin filaments. *eLife* **2**, e00116 (2013).
5. Glotzer, M. The molecular requirements for cytokinesis. *Science (New York, N.Y* **307**, 1735-1739 (2005).
6. Saarikangas, J. & Barral, Y. The emerging functions of septins in metazoans. *EMBO reports* **12**, 1118-1126 (2011
).
7. Bertin, A. *et al.* Phosphatidylinositol-4,5-bisphosphate promotes budding yeast septin filament assembly and organization. *Journal of molecular biology* **404**, 711-731 (2010).
8. Zhang, J. *et al.* Phosphatidylinositol polyphosphate binding to the mammalian septin H5 is modulated by GTP. *Curr Biol* **9**, 1458-1467 (1999).
9. Field, C.M., Coughlin, M., Doberstein, S., Marty, T. & Sullivan, W. Characterization of anillin mutants reveals essential roles in septin localization and plasma membrane integrity. *Development (Cambridge, England)* **132**, 2849-2860 (2005).
10. Kinoshita, M., Field, C.M., Coughlin, M.L., Straight, A.F. & Mitchison, T.J. Self- and actin-templated assembly of Mammalian septins. *Developmental cell* **3**, 791-802 (2002).
11. Oegema, K., Savoian, M.S., Mitchison, T.J. & Field, C.M. Functional analysis of a human homologue of the Drosophila actin binding protein anillin suggests a role in cytokinesis. *The Journal of cell biology* **150**, 539-552 (2000).
12. Joo, E., Surka, M.C. & Trimble, W.S. Mammalian SEPT2 is required for scaffolding nonmuscle myosin II and its kinases. *Developmental cell* **13**, 677-690 (2007).
13. Mostowy, S. *et al.* Entrapment of intracytosolic bacteria by septin cage-like structures. *Cell host & microbe* **8**, 433-444 (2010).
14. Schmidt, K. & Nichols, B.J. A barrier to lateral diffusion in the cleavage furrow of dividing mammalian cells. *Curr Biol* **14**, 1002-1006 (2004).
15. Caudron, F. & Barral, Y. Septins and the lateral compartmentalization of eukaryotic membranes. *Developmental cell* **16**, 493-506 (2009).
16. Liu, J., Fairn, G.D., Ceccarelli, D.F., Sicheri, F. & Wilde, A. Cleavage furrow organization requires PIP(2)-mediated recruitment of anillin. *Curr Biol* **22**, 64-69 (2012).
17. Kechad, A., Jananji, S., Ruella, Y. & Hickson, G.R. Anillin acts as a bifunctional linker coordinating midbody ring biogenesis during cytokinesis. *Curr Biol* **22**, 197-203 (2012).
18. Adam, J.C., Pringle, J.R. & Peifer, M. Evidence for functional differentiation among Drosophila septins in cytokinesis and cellularization. *Molecular biology of the cell* **11**, 3123-3135 (2000).
19. Field, C.M. & Alberts, B.M. Anillin, a contractile ring protein that cycles from the nucleus to the cell cortex. *The Journal of cell biology* **131**, 165-178 (1995).
20. Lecuit, T. & Wieschaus, E. Polarized insertion of new membrane from a cytoplasmic reservoir during cleavage of the Drosophila embryo. *The Journal of cell biology* **150**, 849-860 (2000).

21. Schejter, E.D. & Wieschaus, E. bottleneck acts as a regulator of the microfilament network governing cellularization of the Drosophila embryo. *Cell* **75**, 373-385 (1993).
22. Thomas, J.H. & Wieschaus, E. src64 and tec29 are required for microfilament contraction during Drosophila cellularization. *Development (Cambridge, England)* **131**, 863-871 (2004).
23. Neufeld, T.P. & Rubin, G.M. The Drosophila peanut gene is required for cytokinesis and encodes a protein similar to yeast putative bud neck filament proteins. *Cell* **77**, 371-379 (1994).
24. Field, C.M. *et al.* A purified Drosophila septin complex forms filaments and exhibits GTPase activity. *The Journal of cell biology* **133**, 605-616 (1996).
25. Royou, A., Field, C., Sisson, J.C., Sullivan, W. & Karess, R. Reassessing the role and dynamics of nonmuscle myosin II during furrow formation in early Drosophila embryos. *Molecular biology of the cell* **15**, 838-850 (2004).
26. Fullilove, S.L. & Jacobson, A.G. Nuclear elongation and cytokinesis in Drosophila montana. *Developmental biology* **26**, 560-577 (1971).
27. Carvalho, A., Desai, A. & Oegema, K. Structural memory in the contractile ring makes the duration of cytokinesis independent of cell size. *Cell* **137**, 926-937 (2009).
28. Padash Barmchi, M., Rogers, S. & Hacker, U. DRhoGEF2 regulates actin organization and contractility in the Drosophila blastoderm embryo. *The Journal of cell biology* **168**, 575-585 (2005).
29. Grosshans, J. *et al.* RhoGEF2 and the formin Dia control the formation of the furrow canal by directed actin assembly during Drosophila cellularisation. *Development (Cambridge, England)* **132**, 1009-1020 (2005).
30. Wenzl, C., Yan, S., Laupsien, P. & Grosshans, J. Localization of RhoGEF2 during Drosophila cellularization is developmentally controlled by Slam. *Mechanisms of development* **127**, 371-384 (2010).
31. Zhang, L. & Ward, R.E.t. Distinct tissue distributions and subcellular localizations of differently phosphorylated forms of the myosin regulatory light chain in Drosophila. *Gene expression patterns : GEP* **11**, 93-104 (2011).
32. Kress, A. *et al.* Mapping the Local Organization of Cell Membranes Using Excitation-Polarization-Resolved Confocal Fluorescence Microscopy. *Biophysical journal* **105**, 127-136 (2013).
33. Sirajuddin, M. *et al.* Structural insight into filament formation by mammalian septins. *Nature* **449**, 311-315 (2007).
34. Garcia, G., 3rd *et al.* Subunit-dependent modulation of septin assembly: budding yeast septin Shs1 promotes ring and gauze formation. *The Journal of cell biology* **195**, 993-1004 (2011).
35. Farkasovsky, M., Herter, P., Voss, B. & Wittinghofer, A. Nucleotide binding and filament assembly of recombinant yeast septin complexes. *Biological chemistry* **386**, 643-656 (2005).
36. Weirich, C.S., Erzberger, J.P. & Barral, Y. The septin family of GTPases: architecture and dynamics. *Nature reviews* **9**, 478-489 (2008).
37. Holmes, K.C. Structural biology: actin in a twist. *Nature* **457**, 389-390 (2009).
38. Jansen, S. *et al.* Mechanism of actin filament bundling by fascin. *The Journal of biological chemistry* **286**, 30087-30096 (2011).
39. Faix, J. *et al.* Cortexillins, major determinants of cell shape and size, are actin-bundling proteins with a parallel coiled-coil tail. *Cell* **86**, 631-642 (1996).

40. Bertin, A. *et al.* Saccharomyces cerevisiae septins: supramolecular organization of heterooligomers and the mechanism of filament assembly. *Proceedings of the National Academy of Sciences of the United States of America* **105**, 8274-8279 (2008).
41. Frazier, J.A. *et al.* Polymerization of purified yeast septins: evidence that organized filament arrays may not be required for septin function. *The Journal of cell biology* **143**, 737-749 (1998).
42. Hickson, G.R. & O'Farrell, P.H. Rho-dependent control of anillin behavior during cytokinesis. *The Journal of cell biology* **180**, 285-294 (2008).
43. D'Avino, P.P. *et al.* Interaction between Anillin and RacGAP50C connects the actomyosin contractile ring with spindle microtubules at the cell division site. *Journal of cell science* **121**, 1151-1158 (2008).
44. Estey, M.P., Di Ciano-Oliveira, C., Froese, C.D., Bejide, M.T. & Trimble, W.S. Distinct roles of septins in cytokinesis: SEPT9 mediates midbody abscission. *The Journal of cell biology* **191**, 741-749 (2010).
45. Gilden, J.K., Peck, S., Chen, Y.C. & Krummel, M.F. The septin cytoskeleton facilitates membrane retraction during motility and blebbing. *The Journal of cell biology* **196**, 103-114 (2012).
46. Sedzinski, J. *et al.* Polar actomyosin contractility destabilizes the position of the cytokinetic furrow. *Nature* **476**, 462-466 (2011).
47. Guillot, C. & Lecuit, T. Adhesion disengagement uncouples intrinsic and extrinsic forces to drive cytokinesis in epithelial tissues. *Developmental cell* **24**, 227-241 (2013).
48. Founounou, N., Loyer, N. & Le Borgne, R. Septins Regulate the Contractility of the Actomyosin Ring to Enable Adherens Junction Remodeling during Cytokinesis of Epithelial Cells. *Developmental cell* **24**, 242-255 (2013).
49. Mostowy, S. *et al.* A role for septins in the interaction between the Listeria monocytogenes INVASION PROTEIN InlB and the Met receptor. *Biophysical journal* **100**, 1949-1959 (2011).
50. Tooley, A.J. *et al.* Amoeboid T lymphocytes require the septin cytoskeleton for cortical integrity and persistent motility. *Nature cell biology* **11**, 17-26 (2009).
51. Dagdas, Y.F. *et al.* Septin-mediated plant cell invasion by the rice blast fungus, Magnaporthe oryzae. *Science* **336**, 1590-1595 (2012).
52. Pan, F., Malmberg, R.L. & Momany, M. Analysis of septins across kingdoms reveals orthology and new motifs. *BMC evolutionary biology* **7**, 103 (2007).
53. Sellin, M.E., Sandblad, L., Stenmark, S. & Gullberg, M. Deciphering the rules governing assembly order of mammalian septin complexes. *Molecular biology of the cell* **22**, 3152-3164 (2011).
54. Kim, M.S., Froese, C.D., Estey, M.P. & Trimble, W.S. SEPT9 occupies the terminal positions in septin octamers and mediates polymerization-dependent functions in abscission. *The Journal of cell biology* **195**, 815-826 (2011).
55. Gittes, F., Mickey, B., Nettleton, J. & Howard, J. Flexural rigidity of microtubules and actin filaments measured from thermal fluctuations in shape. *The Journal of cell biology* **120**, 923-934 (1993).
56. Tang, J.X., Kas, J.A., Shah, J.V. & Janmey, P.A. Counterion-induced actin ring formation. *Eur Biophys J* **30**, 477-484 (2001).
57. Taylor, K.A., Taylor, D.W. & Schachat, F. Isoforms of alpha-actinin from cardiac, smooth, and skeletal muscle form polar arrays of actin filaments. *The Journal of cell biology* **149**, 635-646 (2000).

58. Surka, M.C., Tsang, C.W. & Trimble, W.S. The mammalian septin MSF localizes with microtubules and is required for completion of cytokinesis. *Molecular biology of the cell* **13**, 3532-3545 (2002).
59. Kinoshita, M. *et al.* Nedd5, a mammalian septin, is a novel cytoskeletal component interacting with actin-based structures. *Genes & development* **11**, 1535-1547 (1997).
60. Mostowy, S. & Cossart, P. Septins: the fourth component of the cytoskeleton. *Nature reviews. Molecular cell biology* **13**, 183-194 (2012).
61. Lecuit, T. & Pilot, F. Developmental control of cell morphogenesis: a focus on membrane growth. *Nature cell biology* **5**, 103-108 (2003).
62. Murthy, M., Teodoro, R.O., Miller, T.P. & Schwarz, T.L. Sec5, a member of the exocyst complex, mediates Drosophila embryo cellularization. *Development* **137**, 2773-2783 (2010).

FIGURE LEGENDS

Figure 1. Defects in Actomyosin assembly kinetics during cellularization of *septin* mutants. a, Left: Side view of a wild-type embryo during cellularization. Middle: Confocal image of the region outlined in the left panel (white box) showing the localization of Pnut/hSep7 (green), DPatj (magenta) and cell membranes (blue). The FCs are outlined with a white dashed box. Separate panels for each staining at the FCs are shown next to the merged image. Right: Schematic of the FC (lateral cell membranes depicted in black, torus-like geometry of the FC in green). **b,** Confocal images of Myo-II (MRLC), Actin (phalloidin-stained) and Anillin in side views and top views of the FC. Cy, cytoplasm. **c,** Confocal images of Pnut/hSep7 and DSep1 in side views and top views of the FC. **d,** The *Drosophila* septin complex and its human homolog. **e,** Two-photon images of Myo-II during cellularization of wild-type and *septin* mutant embryos. h, depth of membrane invagination. **f,** Quantification of membrane invagination rates (N=6 embryos for each wild-type and mutant, P = 0.0022, Mann-Whitney U test). Error bars are mean ±

SD. **g,** Quantification of membrane invagination depth during cellularization (N=3 depth measurements/timepoint/embryo) **h, i,** Quantification of MRLC::GFP (H) and UtrCHD::GFP (I) intensity during cellularization of wild-type (N=6 FCs/timepoint/embryo) and *septin* mutant (N=3 FCs/timepoint/embryo). Intensities are normalized to the onset of cellularization. Error bars are mean ± SD. Scale bars, 5 μm.

Figure 2. Defects in Actin and Myo-II organization during cellularization of *septin* mutants. a-d, Confocal images from time-lapse imaging of UtrCHD::GFP (a, b) and MRLC::GFP (c, d) during the slow phase. **e, f,** Two-photon images from time-lapse imaging of MRLC::GFP in wild-type (e) and *septin* mutant (f) embryos during the fast phase. **g, i,** Quantification of FC perimeters (g) and circularities, C, (i) from segmentation analysis of wild-type (N=43-134 FCs/timepoint/embryo) and mutant (N=26-118 FCs/timepoint/embryo). All the N numbers of FCs per timepoint per embryo are provided in Supplementary Table 1. Error bars are mean ± SEM. **h, j,** Box plot displaying the distribution of FC perimeters (h) and circularities (j) at 65 min (black arrows in g and i). Box extends from the 25th to the 75th percentile. Whiskers extend to minimum and maximum values. N, number of FCs analyzed. **k,** Confocal images of MRLC, Actin and Anillin in a *septin* mutant. Compare with wild-type in Fig. 1b. N, nucleus. **l,** Localization of Actin and Anillin in side views of a *septin* mutant during slow (1) and fast (2) phase. Compare with wild-type in Fig. 1b. N, nucleus. Scale bars, 5 μm.

Figure 3. Actin organization in *DRhoGEF2* mutants. a-b, Representative confocal images of Actin (phalloidin-stained) and Pnut/hSep7 at the end of cellularization in *DRhoGEF2* mutants (a, 1-3 and b, 1-2 depict different regions of the respective embryo shown in sagittal views). **c,** Representative confocal images of MHC during the fast phase in a wild-type embryo (left) and in *DRhoGEF2* mutants (1,2 depict different regions of the same mutant embryo). Wild-type and *DRhoGEF2* mutant embryos were mixed, fixed, stained, mounted together and imaged under identical conditions. **d,** Confocal images of cellularizing embryos stained with antibodies against total MRLC, pMRLC-S21 and ppMRLC-T20S21. Scale bars in a-d, 5 μm. **e,** Western blots of cellularizing embryos probed with antibodies against the indicated proteins.

Figure 4. Electron microscopy of FCs in wild-type and *septin* mutants. a, Left: Schematic showing the orientation of sections through the FC depicted in the respective panels. Middle: Top view of FCs. Right: Side views of FCs that correspond to the sections shown in the middle panel. **b,** Electron micrographs of FC sections depicting the electron-dense coat (white brackets) that lines the FC membrane. **c,** Electron micrograph of a top view of a wild-type FC depicting the electron-dense coat (white brackets) at the membrane. The inset shows a magnification of the coat (dashed rectangle). **d, e,** Electron micrographs of grazing sections through the sides (d) and the base (e) of the FC in wild-type. White guidelines are oriented parallel to the observed arrays of filaments. **f, g,** Box plot displaying the distribution of FC coat thicknesses (f) and coat densities (g). Box extends from the 25th to the 75th percentile.

Whiskers extend to minimum and maximum values. $P < 2.0\times10^{-6}$. N, number of FC thickness (f) or density (g) measurements.

Figure 5. F-Actin molecular orientational order at the FC is decreased in *septin* mutants. a, Schematic of the molecular orientational order parameters ρ (mean orientation) and ψ (angular aperture). Actin filaments (black box in FC cartoon) are depicted as gray ellipsoids. **b-d, f-h,** Representative composite images of Alexa Fluor phalloidin intensity (grey) and ψ (b-d) or ρ (f-h) angles for wild-type and *septin* mutant, at lateral membranes (b, f) and at the FCs (c, d, g, h). Bottom panels for f-h correspond to the respective dashed boxes in the top panels. Arrowheads point to regions with broad ρ value distributions (f) or where ρ values are not azimuthal at the FC contour (h). **e,** Histograms of ψ. Lateral membranes (ψ in black), wild type: 159° ± 2.5°; FCs (ψ color code as in b), wild type: 140° ± 2.5° (P = 1.0 x 10^{-5}); lateral membranes (ψ in black), *septin* mutant: 160° ± 1.3°; FCs (ψ color code as in b), *septin* mutant: 161° ± 1.5° ($P > 0.2$). **i,** Distribution of ρ angles relative to their average $<\rho>$ within 4x4 pixel regions (white box in cartoon) taken around the contours for wild-type (FCs and lateral membranes) and *septin* mutant (FCs). 20 regions are analyzed for each case. **j,** Representative composite images of Alexa Fluor phalloidin intensity (grey) and ψ angles on stress fibers for two COS-7 cells. The respective histograms of ψ are shown (ψ color code as in b). Left cell, 141° ± 13.5°; right cell, 133° ± 11°). ψ values are mean ± SD. Scale bars, 5 μm.

Figure 6. *In vitro* reconstituted actin filaments are bundled and curved in the presence of septins. a, SDS-PAGE analysis of recombinant septin complexes of His_6-DSep1, DSep2 and Pnut/hSep7-Strep. **b,** Plot of the dependence of the fraction of septins bound (expressed by the bound fraction of DSep2) on the concentration of actin. The K_d (1.2 ± 0.5 μM, N=3) was extracted by fitting the data with a quadratic function. F-Actin in pellets is shown (right top panel). The faint band just below the band of Actin, evident at low Actin concentrations, corresponds to DSep1. Septin depletion (DSep2) from the supernatant with increasing actin concentrations is shown (right bottom panel). Error bars are mean ± SD. **c,** Low speed co-sedimentation of 1 μM F-actin co-polymerized with 1 μM Fascin or 1 μM fly septins. Western blots for Actin are shown (the displayed fractions have been selected from the respective gels shown in Supplementary Fig. 4a,b). T, total. S, supernatant. P, pellet. **d,** Representative TIRF images of *in vitro* reconstituted AF488-actin filaments at 1 μM in the absence of cross-linkers and co-polymerized with fly septins, human septins, or Fascin at 0.1 μM each. **e,** Representative TIRF images of *in vitro* reconstituted AF594-actin filaments at 1 μM co-polymerized with AF488-fly septins at 0.1 μM. Scale bars, 5 μm.

Figure 7. Negative-stain EM of *in vitro* reconstituted actin filaments in the presence of septins. a, b, Electron micrographs of reconstituted F-actin (a) and purified *Drosophila* septin complexes (b) at the indicated protein and salt concentrations. **c,** Representative two-dimensional class averages of purified *Drosophila* septin complexes (DSC) in solution. Different orientations

of the hexameric complexes are shown where the different faces of the septin complex can be seen. **d-f,** Electron micrographs of reconstituted F-actin co-polymerized with purified *Drosophila* septins. Images correspond to different combinations of F-actin and septin concentrations. d, 3 μM F-actin and 0.5 μM septins. e, 12 μM F-actin and 0.6 μM septins. f, 3 μM F-actin and 0.3 μM septins. Black dots within the black outlined boxes in e and f indicate single actin filaments, and white arrowheads in f point to periodic striations. **g,** Electron micrographs of reconstituted F-actin (1 μM) co-polymerized with *Drosophila* septins (1 μM). Proteic decoration can be seen along the actin bundle, and septin hexamers are present around the actin bundle. **h,** Electron micrographs of reconstituted F-actin (2 μM) co-polymerized with septins (0.5 μM) and stained with Ni-NTA-Nanogold particles that bind His-tagged DSep1. Black dots correspond to gold particle decoration. Two different examples of stained bundles are shown.

Figure 8. F-actin bundle formation in the presence of septin hexamers or preformed septin bundles. a, Representative TIRF image of AF488-fly septin bundles. **b,** Representative low- and high-magnification EM images of fly septin bundles formed at 0.5 μM (left) or 1 μM (right). **c,** Representative TIRF images of preformed AF488-fly septin bundles (1 μM) mixed with AF594-G-actin (1 μM). Red and white arrowheads point to curved and straight actin bundles (Actin panel) and the corresponding septin signal (septin panels), respectively. Gray values are displayed in the same grayscale range for each pair of top and bottom panels. Scale bars, 5 μm. **d,** Time-lapse

imaging of actin bundle formation in the presence of 0.1 μM fly septins. Red, black and blue arrowheads point to the sequential formation of bends as actin filaments polymerize and form bundles. Compare with **e** for single actin filaments. The selected snapshots correspond to Supplementary Video 3. Scale bar, 5 μm. **e,** Time-lapse imaging of thermally undulating actin filaments. The black arrow points to a single actin filament. The selected snapshots correspond to Supplementary Video 4. Scale bar, 5 μm. **f,** Model of how septins affect actin filament organization *in vivo*. Left, Schematic of the FC (lateral membranes in black, torus-like geometry of the membrane front in green). Right, A section is shown through the membrane at the FC for wild type (top) and *septin* mutants (bottom). Septins bundle and bend actin filaments in wild type, seen as organized, tightly-packed filament bundles by EM and polarization fluorescence microscopy. Actin filaments are loosely packed and disorganized in the *septin* mutant, with no detectable organized and ordered structure by EM and polarization fluorescence microscopy. Remaining actin filaments at the membrane in *septin* mutants are cross-linked and bound to the membrane through Anillin [16].

SUPPLEMENTARY FIGURE LEGENDS

Supplementary Figure 1. FC membrane polarity is not affected during cellularization of *septin* mutants. a, b, Confocal images of DSep1 (a, left) and DSep2 (b, left) in a top view of the FC in a wild-type embryo. Side views of the FC in wild-type and *septin* mutant depicting the localization of the lateral membrane marker, Scb, and DSep1 (a, right) and Scb and DSep2 (b, right). **c,** Confocal images of the lateral membrane marker, Dlg, and the FC membrane markers, DPatj, Slam and DRhoGEF2, in side views of the FC during the fast phase of wild-type and *septin* mutant embryos. Notice the flat morphology of FC membranes in mutants (arrowheads). **d,** Confocal images of DPatj and Dlg in a top view of the FC during the fast phase of wild-type and *septin* mutant embryos. A higher magnification of a FC in the mutant (dashed box) shows the segregation of Dlg and DPatj. **e,** Localization of myosin heavy chain (MHC), Pnut/hSep7 and DSep1 at the FC of *septin* mutant embryos. A higher magnification of the FC region is depicted on the right. **f,** Two-photon images of UtrCHD::GFP during cellularization of wild-type (top panel) and *septin* mutant (bottom panel). Scale bars, 5 μm.

Supplementary Figure 2. Defects in F-actin organization during cellularization of *septin* mutants. a, c, d, Confocal images of Actin (phalloidin-stained) during the early slow phase (A, 1-3 depict three representative examples), the early fast phase (C, 1-2 depict two representative examples) and the late fast phase (D, right) of *septin* mutants. Actin in wild type embryos of the respective stages are shown in c and d, left

for comparison. **b,** Side view of FCs in a *septin* mutant stained for Actin, MHC and Pnut/hSep7. **e,** Quantification of FC perimeters from segmentation analysis of wild-type (N=32-144 FCs/timepoint/embryo) embryos. All the N numbers of FCs per timepoint per embryo are provided in Supplementary Table 1. Constriction rates are calculated from linear regression analysis in the regions depicted by the two black line segments. Error bars are mean ± SD. **f,** Definition of circularity. Scale bars, 5 μm.

Supplementary Figure 3. Electron microscopy of FCs in wild-type and *septin* mutants. a, Electron micrograph of a FC section depicting how measurements of FC coat densities (quantified in Fig. 4g) were performed. I, Mean pixel intensity. **b,** Examples of FC sections in wild-type and *septin* mutants at low magnification. **c,** Electron micrograph of grazing sections through the side of a FC in a wild-type (left) and a *septin* mutant (right). The schematic depicts the grazing sections with respect to the FC geometry. Dashed black lines follow the FC membrane contour. White guidelines in wild-type are oriented parallel to the observed arrays of filaments. **d,** Electron micrograph of a top view of a wild-type FC depicting the curved electron-dense coat (white brackets) at the membrane **e,** Electron micrograph of a grazing section through the base of a wild-type FC. White guidelines are oriented parallel to the observed arrays of filaments.

Supplementary Figure 4. *In vitro* reconstituted actin filaments are bundled in the presence of septins. a, b SDS-PAGE analysis (Coomassie

blue stained) of fractions from low speed co-sedimentation of 1 μM F-actin co-polymerized with the indicated concentrations of Fascin (a) or *Drosophila* septins (b). T, total. S, supernatant. P, pellet.

Supplementary Figure 5. Characterization of DSep1 and DSep2 antibodies generated in this study. a, b, Homology models of DSep1 (a) and DSep2 (b) structures depicting in red the amino acid (aa) sequence and respective regions in the structure that were used as epitopes for antibody production. **c, d,** Western blot of purified recombinant septin complexes (c) and wild-type embryo lysates (d) using the DSep1 and DSep2 antibodies generated in this study. **e,** SDS-PAGE analysis of recombinant septin complexes of His_6-hSep2, hSep6 and hSep7-Strep.

Supplementary Figure 6. Representative entire images of immunoblotting and SDS-PAGE. Boxed areas were cropped for designated figures. Dotted lines denote separations of membranes for dual labeling.

SUPPLEMENTARY VIDEO LEGENDS

Supplementary Video 1. Side view of membrane invagination during cellularization in a MRLC::GFP expressing wild-type and *septin* mutant embryo, imaged with two-photon microscopy. Time interval between acquired frames was 2 min and the acquisition length was 90 min (wild-type) and 98 min (mutant). Video is 706 x faster than real-time.

Supplementary Video 2. Top view of a MRLC::GFP expressing wild-type and *septin* mutant embryo during the slow phase of cellularization. Images were collected at the FC with spinning disk confocal microscopy. Time interval between acquired frames was 10 s and the acquisition length was 44 min. Video is 149 x faster than real-time.

Supplementary Video 3. Time-lapse imaging of actin bundle formation in the presence of 0.1 μM fly septins. Time interval between acquired frames was 0.5 s and the acquisition length was 5 min. Video is 7.5 x faster than real-time.

Supplementary Video 4. Time-lapse imaging of thermally undulating single actin filaments. Time interval between acquired frames was 0.5 s and the acquisition length was 1 min. Video is 7.5 x faster than real-time.

METHODS

Fly stocks and genetics. *yellow white* flies were used as a control. [UASp-GAP43::mVenus, nanosGal4] (III) [63] (Fig. 1a), *sqh*^{AX3}; sqh-MRLC::GFP; sqh-MRLC::GFP [25] and sqh-UtrCHD::GFP (III) [64] are described in the indicated references. To remove maternally contributed *pnut* product, we used the FLP-DFS system to generate germline clones homozygous for the molecular null allele *pnut*^{XP} [18,23]. To visualize Myo-II and Actin we generated hsFLP^{12}; FRT^{2R-G13}, *pnut*^{XP}/CyO; sqh-MRLC::GFP and hsFLP^{12}; FRT^{2R-G13}, *pnut*^{XP}/CyO; sqh-UtrCHD::GFP stocks and used them for control MRLC::GFP and UtrCHD::GFP intensity measurements, or in crosses to produce germline clones. For the sake of simplicity we refer to *pnut*^{XP} germline clone embryos as *septin* mutants. FRT^{2R-G13}, *DRhoGEF2*$^{l(2)04291}$ (a null allele) was a gift from U. Häcker. Data regarding *DRhoGEF2* mutants were from embryos derived from females carrying *DRhoGEF2*$^{l(2)04291}$ germline clones crossed with heterozygous males.

Antibody generation. To generate specific antibodies for DSep1 and DSep2, peptides corresponding to the N-terminal regions of DSep1 and DSep2 (Supplementary Fig. 5a,b) were commercially synthesized and used to immunize rats (for DSep1) or guinea pigs (for DSep2) at Eurogentec. The sequences used were MADTKGFSSIETPGY and LKQSGHVGFDSLPDQ for DSep1 and DSep2, respectively. Anti-DSep1 and anti-DSep2 antibodies were affinity purified and their specificity tested in Western blots (Supplementary Fig. 5c,d) and immunostainings (Fig. 1 and Supplementary Fig. 1). Homology modeling of DSep1 and DSep2 (Supplementary Fig. 5a,b) was carried out

using HHpred (http://toolkit.tuebingen.mpg.de/hhpred/) and the structures of hSep2 and the hSep2-hSep6-hSep7 trimer, respectively.

Immunofluorescence of embryos. Embryos were 4% formaldehyde-methanol fixed and labeled with mouse 4C9H4 anti-Pnut (1:3, DSHB), mouse 4F3 anti-Dlg (1:300, DSHB), rabbit anti-Scb (1:2,500, a gift from C. Doe), rabbit anti-DPatj (1:1,000, a gift from H. Bellen), rabbit anti-MHC (1:250, Lecuit lab), rabbit anti-Anillin (1:1,200, a gift from C. Field), rat anti-DSep1 (1:250), guinea pig anti-DSep2 (1:250), mouse anti-MRLC (1:1000, a gift from R. Ward), guinea pig anti-pMRLC-S21 (1:100, a gift from R. Ward) and rat anti-ppMRLC-T20S21 (1:1000, a gift from R. Ward). Heat-methanol fixation was used for rabbit anti-Slam (1:1,000, a gift from R. Lehmann) and guinea pig anti-DRhoGEF2 (1:500, a gift from J. Grosshans). For MRLC and GAP43 stainings, MRLC::GFP and GAP43::mVenus [63] expressing embryos were formaldehyde-methanol fixed and labeled with chicken anti-GFP (1:1000, Aves Labs #1020). Secondary antibodies (Invitrogen) were used at 1:500. Embryos were 8% formaldehyde fixed and hand-devitellinized for F-actin stainings with Alexa Fluor 546 phalloidin (1:50, Invitrogen). Embryos were mounted with Aqua-Poly/Mount (Polysciences). Confocal images were acquired with a Zeiss Plan-Apochromat 63x/1.4 NA oil or Plan-Neofluar 100x/1.3 oil objective on a Zeiss 510 Meta microscope.

Western blots of cellularizing embryos. For pMRLC, embryos were fixed in formaldehyde 37% : heptane 1:1 for 5 min, rinsed with PBS/BSA 0.1%/Tween20 0.1% and hand-devitellinized. Cellularizing embryos were selected, crushed in lysis buffer (25 mM Tris-HCl pH 8, 27.5 mM NaCl, 20 mM

KCl, 25 mM sucrose, 10 mM Na-EDTA pH 8, 10 mM Na-EGTA pH 8, 10% glycerol, 0.5% NP-40, 1 mM DTT, 1 mM PMSF, Complete protease inhibitor cocktail (Roche), 20 mM NaF, 2 mM sodium pyrophosphate, 2 mM sodium orthovanadate and 20 mM β-glycero-phosphate) and boiled in Laemmli buffer. The equivalent of 15 embryos (out of which 11 in slow phase and 4 in fast phase) were loaded per lane. For MHC and tubulin (used as a loading control), embryos were lysed directly before boiling in Laemmli buffer for 5 min. Standard procedures were used for Western blotting using an Immobilon-P membrane (0.45 μm, Millipore) and Blotto nonfat dry milk (sc-2325, Santa Cruz). Blocking and primary antibody incubations were in 5% milk in TBS-T/50 mM NaF and secondary antibodies in 1% milk in TBS-T/50 mM NaF. Primary antibodies were mouse anti-tubulin (1:1000, Sigma, T9026, clone DM1A), rabbit anti-MHC (1:2000, Lecuit lab) and rabbit anti-pMRLC-S19 (1:50, Cell Signaling, #3671). Secondary antibodies were mouse and rabbit HRP-conjugated from GE Healthcare (NA9310 and NA9340) at 1:2,000. Standard ECL imaging was used for detection.

Live embryo time-lapse imaging. Embryos were imaged at 19°C as detailed in[65]. Images were acquired on a Nikon spinning disc confocal Eclipse Ti inverted microscope with a 100x/1.4 NA oil objective, a 491-nm diode laser and a Photometrics EMCCD camera (133 nm/pixel). Z-stacks were collected every 10 s with a z-stack spacing of 0.5 μm (Fig. 2a-d). For two-photon microscopy, images were acquired on a Nikon A1R-MP upright microscope with a 25x/1.1 NA water immersion objective, a 940-nm Mai Tai Deepsee laser and a PMT detector. Sagittal planes for membrane depth and

MRLC::GFP/UtrCHD::GFP intensity measurements were collected every 2 min at 80-100 μm deep from the embryo surface (Fig. 1e and Supplementary Fig. 1f). Top views of the furrow canal for segmentation analysis were collected as z-stacks of three planes every 2 min with a z-stack spacing of 0.5 μm (Fig. 2e,f).

Transmission electron microscopy of embryos. Embryos were prepared as detailed in [66]. FC sections were examined in 10 wild-type and *septin* mutant embryos each, and at least 20 FCs were imaged per embryo. FC thickness and density were measured during the fast phase of cellularization. FC thickness was measured in different regions (sides and base) for each FC, and minimum and maximum thickness values for each FC were plotted. Measurements of FC coat densities (Fig. 4g) are reported using a lookup table where black corresponds to a gray value of 0 and white to a gray value of 255. At least 10 grazing sections at the sides or at the bases of FCs (Fig. 4a, sections *d* and *e*) in wild-type and *septin* mutants each were imaged, and the images shown in Fig. 4d,e and Supplementary Fig. 3c,e are representative.

Image analysis and quantification. Images were processed with ImageJ and Fiji freeware and prepared with Adobe Illustrator. Images from immunostainings are from single planes in sagittal sections and from maximum intensity z projections in top views. Images from spinning disk microscopy are from maximum intensity z projections in top views (Fig. 2a-d). TIRF and confocal images of reconstituted F-Actin are from single planes. The contrast of TIRF and confocal images presented in Fig. 6 and Fig. 8 has been adjusted post acquisition so that both dim and bright structures are

visible. A Gaussian smoothing filter with a radius of one pixel was used to reduce noise in presented images.

Membrane depth, MRLC::GFP and UtrCHD::GFP intensity measurements were from single planes in sagittal sections. Mean membrane depth (Fig. 1g) was calculated from three measurements between the apex of the forming cells and the base of the furrow canal in MRLC::GFP embryos. Mean MRLC::GFP and UtrCHD::GFP intensities (Fig. 1h,i) were measured in regions that encompassed discrete furrow canals and did not contain the adjacent adherens junction region. To define the time from the onset of cellularization (Fig. 1h,i), membrane depth at each timepoint was compared to mean depth measurements over time for the respective genotype (Fig. 1g) and time was accordingly calculated.

Furrow canal perimeter and circularity (Fig. 2g,i) were extracted from segmentation analysis of maximum intensity z projections of three planes in top views (Fig. 2e,f). Image segmentation was carried out with the Motiontracking II program (Kalaimoscope). To define the time that corresponds to each z-stack in top views, sagittal planes were collected between successive z-stacks and used for time assignment based on membrane depth measurements. Constriction rates (Supplementary Fig. 2e) were calculated from segmented images using the extracted perimeter values at each timepoint. The number of segmented FCs in Fig. 2g,i and Supplementary Fig. 2e is given as a range due to the varying number of FCs that are succesfully segmented in the imaged region for each timepoint. All

the N numbers of FCs per timepoint per embryo are provided in Supplementary Table 1.

Polarization resolved fluorescence microscopy. Polarization resolved fluorescence measurements were performed on a confocal microscope using a water immersion objective lens (C-Apochromat 40x UV-VIS-NIR, NA=1.2, Carl Zeiss) as detailed in [32]. The excitation power at the entrance of the objective lens was 8 μW. Galvanometric mirrors provided a series of 30 μm x 30 μm or 20 μm x 20 μm images (150x150 pixels, 100 μs per pixel) for an incident polarization angle varying between 0° (with respect to the horizontal in the image plane) and 180°, every 6°. Polarization-resolved data analysis was according to [32]. The retrieved quantities per pixel are the mean orientation angle of the molecular angular distribution (angle ρ) and its aperture (angle ψ). For each wild-type and *septin* mutant, images were acquired in top views of fast phase cellularizing embryos at sections through the lateral membranes and through the furrow canals. In each case four different embryos were imaged, leading to about 100 furrow canal / polygon (lateral membranes) contours each for wild-type and mutant. Only pixels representative of the furrow canal/polygon membrane contours are analyzed (each furrow canal/polygon contour contains about 300 analyzed pixels). Histograms of ψ are represented for the whole collection of measured pixels, and statistical values (mean ψ, SD ψ, *P* values) are given for compared regions. Statistical significance was determined and *P* values calculated with an ANOVA One-way Tukey HSD test. COS-7 cells were cultured under standard conditions. Cells were fixed (4% paraformaldehyde, 0.5% Triton X-

100, 2% BSA, 1h at 4°C) and stained with Alexa 488 phalloidin (1 nM for 20,000 cells, 30 min at 4°C), washed with 0.1% Tween-20. Measurements were performed at RT in phosphate-buffered saline.

Expression and purification of recombinant *Drosophila* septin complexes. Full-length cDNAs encoding Pnut/hSep7, DSep1 and DSep2 were obtained from DGRC. A two-tag purification scheme was designed in order to select for complexes with full-length Pnut/hSep7 and to minimize isolation of substoichiometric septin complexes. A Strep-tag (WSHPQFEK) was introduced through PCR to the C-terminus of Pnut/hSep7. The cDNA of DSep1 was cloned into pnEA-vH (to introduce an N-terminal His-tag), and cDNAs of DSep2 and Pnut/hSep7-Strep were cloned into pnCS for dual expression following the multi-expression cloning strategy detailed in [67]. Generated plasmids were verified by sequencing.

Co-expression of His_6-DSep1, DSep2 and Pnut/hSep7-Strep was achieved by co-transforming the two plasmids into *E.coli* BL21(DE3). Cotransformants were grown at 37°C in Terrific Broth medium containing ampicillin and spectinomycin to A_{600nm}=2-3, expression was induced with 1 mM IPTG for 1 h at 37°C and cells were harvested and frozen at –80°C for storage or were used for further purification. Cells were resuspended in 50 mM Tris-HCl pH 8, 500 mM KCl, 10 mM imidazole, 5 mM $MgCl_2$, 0.25 mg/mL lysozyme, 1 mM PMSF, Complete protease inhibitor cocktail (Roche), 0.01 g/L DNase and 20 mM $MgSO_4$ and lysed by sonication. The lysate was clarified by centrifugation at 20,000 g for 30 min at 4°C, and the supernatant loaded on a HisTrap FF crude column (GE Healthcare) equilibrated with 50 mM Tris-HCl pH 8, 500

mM KCl, 10 mM imidazole pH 8 and 5 mM $MgCl_2$. His_6-DSep1 containing complexes were eluted with 50 mM Tris-HCl pH 8, 500 mM KCl, 250 mM imidazole pH 8 and 5 mM $MgCl_2$. The eluate was then loaded to a StrepTrap HP column (GE Healthcare) equilibrated with 50 mM Tris-HCl pH 8, 300 mM KCl and 5 mM $MgCl_2$, and Pnut/hSep7-Strep containing complexes were eluted with 50 mM Tris-HCl pH 8, 300 mM KCl, 5 mM $MgCl_2$ and 2.5 mM desthiobiotin. The eluate was then subjected to size exclusion chromatography on a Superdex 200 HiLoad 16/60 equilibrated with 50 mM Tris-HCl pH 8, 300 mM KCl, 5 mM $MgCl_2$ and 5 mM dithiothreitol, and the complex was eluted in the same buffer. All purification steps were performed at 4°C.

The eluted fractions were analyzed by 12% SDS-PAGE, and protein integrity was further tested with Western blots using HRP-conjugated anti-Penta-His (1:10,000, Qiagen), mouse 4C9H4 anti-Pnut (1:100, DSHB), rat anti-DSep1 (1:500) and guinea pig anti-DSep2 (1:500) and ECL detection. Purified septin complexes were flash-frozen in liquid nitrogen and stored at –80°C, or concentrated using passivated (5% Triton X-100) Amicon concentrators before flash-freezing and storage. Alexa Fluor 488-septin conjugates were prepared with Alexa Fluor 488 succinimidyl ester according to the manufacturer's protocol (Invitrogen).

The purity of different septin preps was assayed by mass spectrometry, both in solution (Nano-HPLC-MS/MS (Orbitrap)) to get the whole peptide composition and from protein bands excised from gels (MALDI-TOF MS). The only protein identified besides septins was the bacterial chaperone DnaK

which ran as a faint band just above full-length Pnut in SDS-PAGE (Fig. 6a, Supplementary Fig. 4b, supernatant) and which consistently stayed in the supernatant in co-sedimentation assays (Supplementary Fig. 4b, supernatant). Faint bands running below full-length Pnut were identified as Pnut (Fig. 6a, Supplementary Fig. 4b, also confirmed by Western blots).

Expression and purification of recombinant human septin complexes. Full-length cDNAs encoding hSep2, hSep6 and hSep7 were a gift from A. Wittinghofer. A Strep-tag was introduced through PCR to the C-terminus of hSep7. The cDNA of hSep2 was cloned into pnEA-vH and cDNAs of hSep6 and hSep7-Strep were cloned into pnCS for dual expression [67]. Generated plasmids were verified by sequencing. Co-expression of His_6-hSep2, hSep6 and hSep7-Strep and purification of septin complexes were as described for *Drosophila* septins. Protein integrity was tested with Western blots using goat anti-hSep2 (1:500, Santa Cruz Biotechnology, sc-20408), rabbit anti-hSep6 (1:500, Santa Cruz Biotechnology, sc-20180) and rabbit anti-hSep7 (1:200, Santa Cruz Biotechnology, sc-20620).

Low-speed co-sedimentation assays. G-actin was purified from skeletal rabbit muscle by standard procedures including a final gel filtration step on a HiPrep Sephacryl S-200 26/60 HR (GE Healthcare)[68]. G-actin was stored at –80°C in G-buffer (2 mM Tris-HCl, 0.2 mM Na_2ATP, 0.2 mM $CaCl_2$, 2 mM dithiothreitol (DTT), pH 7.8). Before use, G-actin, Fascin and septins were cleared for 5 min at 120,000 g at room temperature in a Beckman airfuge. G-actin was then polymerized in the presence or absence of Fascin or septins for 30-45 min at room temperature in polymerization buffer (20 mM imidazole-

HCl pH 7.4, 1 mM DTT, 0.1 mM MgATP, 50 mM KCl and 2 mM $MgCl_2$). Samples (100 μL) were sedimented for 15 min at 12,000 g at room temperature in an Eppendorf centrifuge. Pellets were brought to the original volume in polymerization buffer. Proteins in pellets and supernatants were analyzed by standard SDS-PAGE and Coomassie-blue stain. The same fractions were used in Western blots with mouse anti-Actin from Sigma (A3853, clone AC-40) at 1:10,000 and HRP-conjugated secondary antibodies from GE Healthcare (NA9310) at 1:2,000.

High-speed co-sedimentation assays. Actin at increasing concentrations was co-polymerized with *Drosophila* septins (fixed at 1.0 μM) for 2 hous at room temperature. Samples were centrifuged at 120,000 g for 1 hour at room temperature. Pellets were brought to the original volume with polymerization buffer. Proteins in supernatants and pellets were analyzed by SDS-PAGE, stained with Coomassie Blue, and gels scanned to measure the fraction of septins bound. Plots of the dependence of the fraction of septins bound on the concentration of actin from 3 independent experiments were fit with a quadratic function[69] to yield the K_d.

***In vitro* reconstitution of F-actin for fluorescence microscopy.**

Preparation of flow cells. Microscope slides and coverslips were cleaned for 30 min in base-piranha solution and stored in 100% isopropanol. Flow cells were assembled by sandwiching strips of Parafilm between clean glass substrates and melting at 120°C. The resulting chambers were passivated by incubating for 15 min with 1 M potassium hydroxide, rinsing with Milli-Q water, blow-drying with nitrogen gas, incubating for 45 min with 0.2 mg/mL poly-L-

lysine-polyethylene-glycol (Surface Solutions), rinsing with Milli-Q water, and blow-drying with nitrogen gas. Actin solutions were loaded into flow cells and sealed with VALAP.

Protein Preparation. Lyophilized actin (Cytoskeleton) was resuspended to 5 mg/mL in G-buffer and stored at –80°C. Frozen aliquots were thawed, treated with 5 mM DTT, centrifuged at 120,000 g for 30 min in a Beckman airfuge, and sonicated for 5 min to remove actin dimers. Fluorescently labeled actin was purified from skeletal rabbit muscle and labeled with Alexa Fluor-488 or -594 (Invitrogen) [70]. Recombinant GST-tagged mouse Fascin (the plasmid was a gift from S. Hansen and R.D. Mullins) was produced in *E.coli* and purified using standard procedures.

Sample preparation for fluorescence microscopy. Labeled actin monomers were mixed with unlabeled actin monomers to 10% label-monomer molar ratio before polymerization. Actin was polymerized by mixing actin monomer solutions with a solution containing buffer, salts, and Fascin or septins. For septin decoration experiments, labeled septins were mixed with unlabeled septins to 4% label-monomer molar ratio before polymerization. Samples were mixed to yield the final composition of polymerization buffer additionally containing 1 mM Trolox, 2 mM protocatechuic acid, 0.1 μM protocatechuate 3,4-dioxygenase, and 0.1% (w/v) methylcellulose. For TIRF experiments, samples were imaged with a Nikon Apo TIRF 100x/1.49 NA oil objective mounted on an Eclipse Ti microscope (Nikon) using 491 nm and 561 nm laser lines and imaged with a QuantEM 512SC EMCCD camera (Photometrics). For confocal experiments, samples were imaged with a Nikon

Apo TIRF 100x/1.49 NA oil objective mounted on an Eclipse Ti microscope (Nikon) using 488 nm and 561 nm laser lines and imaged with an A1 PMT detector unit (Nikon).

Transmission electron microscopy of reconstituted F-actin. Commercial actin (Cytoskeleton) was polymerized at the desired concentration and prepared as described below. Septins were diluted to the desired concentration either in gel filtration buffer (300 mM KCl) or to 50 mM KCl, immediately adsorbed on grids and prepared as described below. To probe the effect of septins on actin organization, actin was co-polymerized with septins in polymerization buffer for at least three hours at room temperature. Carbon-coated copper grids (CF300-Cu, Electron Microscopy Sciences) were glow discharged before the protein solutions were adsorbed onto the grids. Samples were incubated for at least an additional 30 minutes on grids in a humid environment. The samples were stained with Nano-W (Nanoprobes) and examined with either a JEOL 1400 (120 kV) electron microscope at Imagif (Gif sur Yvette, France) equipped with a SC100 Orius CCD camera or with a Philips CM12 (120 kV) electron microscope at Imagopole (Institut Pasteur, France). For image processing, images were collected on a JEOL 2010F (200kV) microscope with a CCD ultrascan 4K X 4K camera (Institut Pasteur, France). For 2D analysis of septin complexes, 60 images of septins at 0.5 µM in 300 mM KCl were collected at a magnification of 50,000 and a pixel size of 2.2 Å. 3,707 particles were windowed out using the Boxer interface of Eman. Two dimensional processing was carried out with SPIDER[40]. To label septins within F-actin bundles, 5 nm Ni-NTA-Nanogold (Nanoprobes) was used. Actin and septins were co-polymerized and

adsorbed to grids as described above, grids were incubated with undiluted gold particles for 1 min, washed into ten successive drops of water and stained with Nano-W.

Statistics. All error bars are mean ± SD unless otherwise indicated. Statistical significance was determined and *P* values calculated with a non-parametric Mann-Whitney U test. No statistical method was used to predetermine sample size. The experiments were not randomized, and the investigators were not blinded to allocation during experiments and outcome assessment.

Repeatability.

All experiments that were used for quantification were repeated at least three times and up to six times. All remaining experiments, representative images of which are shown in Fig. 1-8 and Sup. Fig. 1-5, were repeated at least twice and up to ten times.

SUPPLEMENTARY REFERENCES

63. Mavrakis, M., Rikhy, R. & Lippincott-Schwartz, J. Plasma membrane polarity and compartmentalization are established before cellularization in the fly embryo. *Developmental cell* **16**, 93-104 (2009).
64. Rauzi, M., Lenne, P.F. & Lecuit, T. Planar polarized actomyosin contractile flows control epithelial junction remodelling. *Nature* **468**, 1110-1114 (2010).
65. Mavrakis, M., Rikhy, R., Lilly, M. & Lippincott-Schwartz, J. Fluorescence imaging techniques for studying Drosophila embryo development. *Current protocols in cell biology / editorial board, Juan S. Bonifacino ... [et al* **Chapter 4**, Unit 4 18 (2008).
66. Levayer, R., Pelissier-Monier, A. & Lecuit, T. Spatial regulation of Dia and Myosin-II by RhoGEF2 controls initiation of E-cadherin endocytosis during epithelial morphogenesis. *Nature cell biology* **13**, 529-540 (2011).
67. Diebold, M.L., Fribourg, S., Koch, M., Metzger, T. & Romier, C. Deciphering correct strategies for multiprotein complex assembly by co-expression: application to complexes as large as the histone octamer. *Journal of structural biology* **175**, 178-188 (2011).
68. Pardee, J.D. & Spudich, J.A. Purification of muscle actin. *Methods in enzymology* **85 Pt B**, 164-181 (1982).

69. Pollard, T.D. A guide to simple and informative binding assays. *Molecular biology of the cell* **21**, 4061-4067 (2010).
70. Gentry, B.S. *et al.* Multiple actin binding domains of Ena/VASP proteins determine actin network stiffening. *Eur Biophys J* (2012).

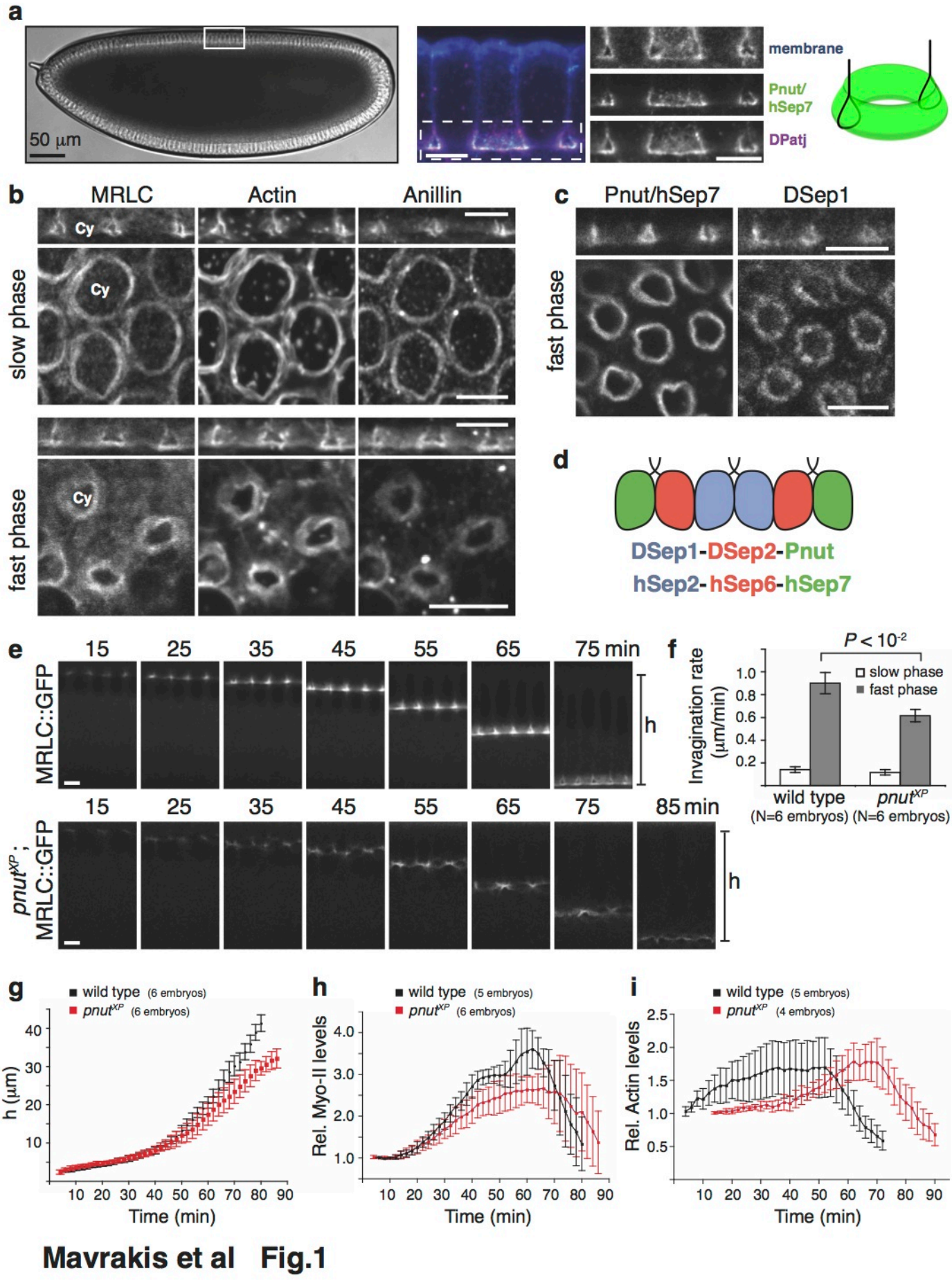

Mavrakis et al Fig.1

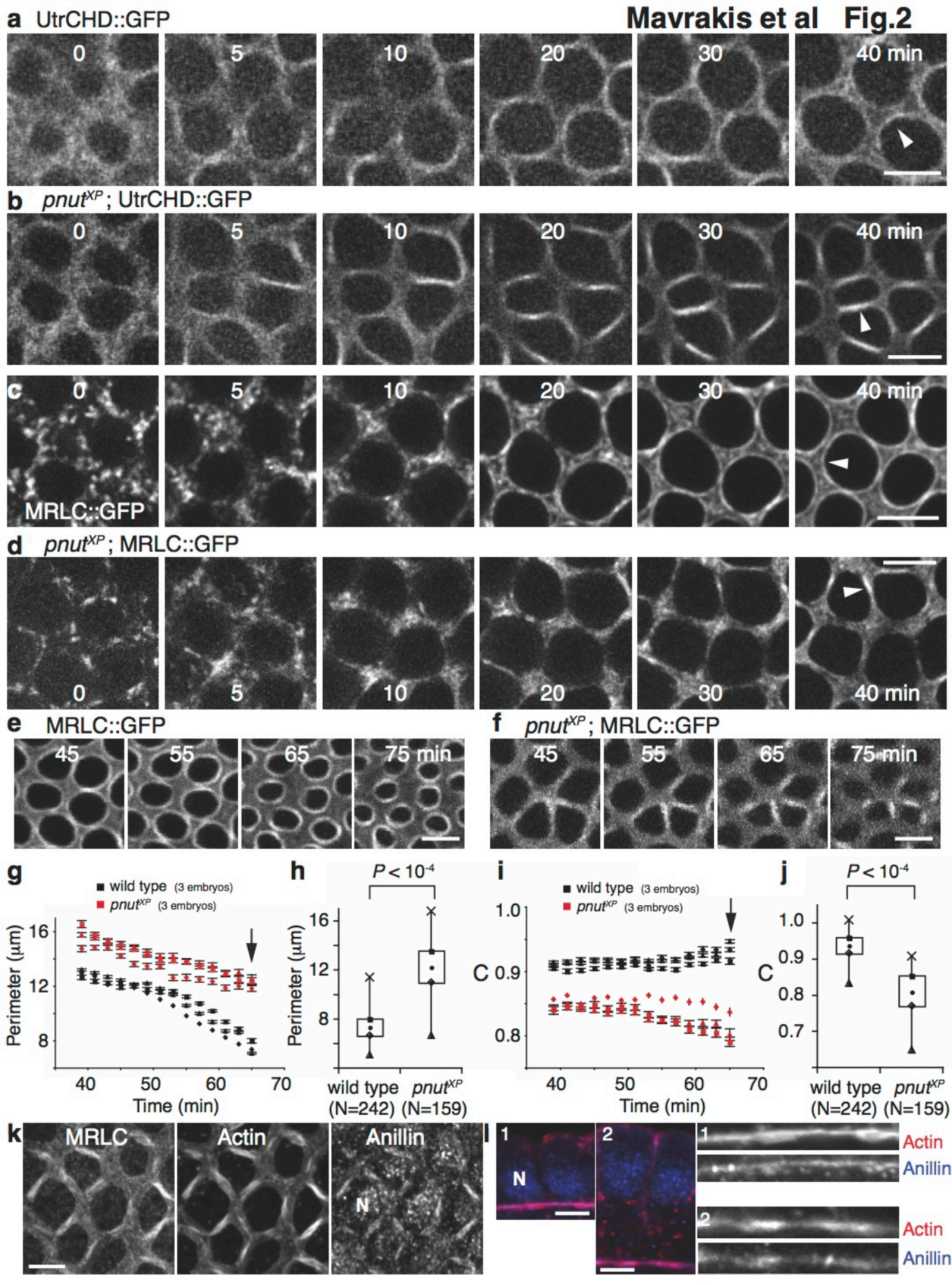
a UtrCHD::GFP
0
5
10
20
30
40 min
b pnutXP; UtrCHD::GFP
0
5
10
20
30
40 min
c
0
5
10
20
30
40 min
MRLC::GFP
d pnutXP; MRLC::GFP
0
5
10
20
30
40 min
e MRLC::GFP
45
55
65
75 min
f pnutXP; MRLC::GFP
45
55
65
75 min
g
wild type (3 embryos)
pnutXP (3 embryos)
Perimeter (μm)
16
12
8
40
50
60
70
Time (min)
h
P < 10-4
Perimeter (μm)
16
12
8
wild type (N=242)
pnutXP (N=159)
i
wild type (3 embryos)
pnutXP (3 embryos)
C
1.0
0.9
0.8
40
50
60
70
Time (min)
j
P < 10-4
C
1.0
0.9
0.8
0.7
wild type (N=242)
pnutXP (N=159)
k
MRLC
Actin
Anillin
N
l
1
N
2
1
Actin
Anillin
2
Actin
Anillin

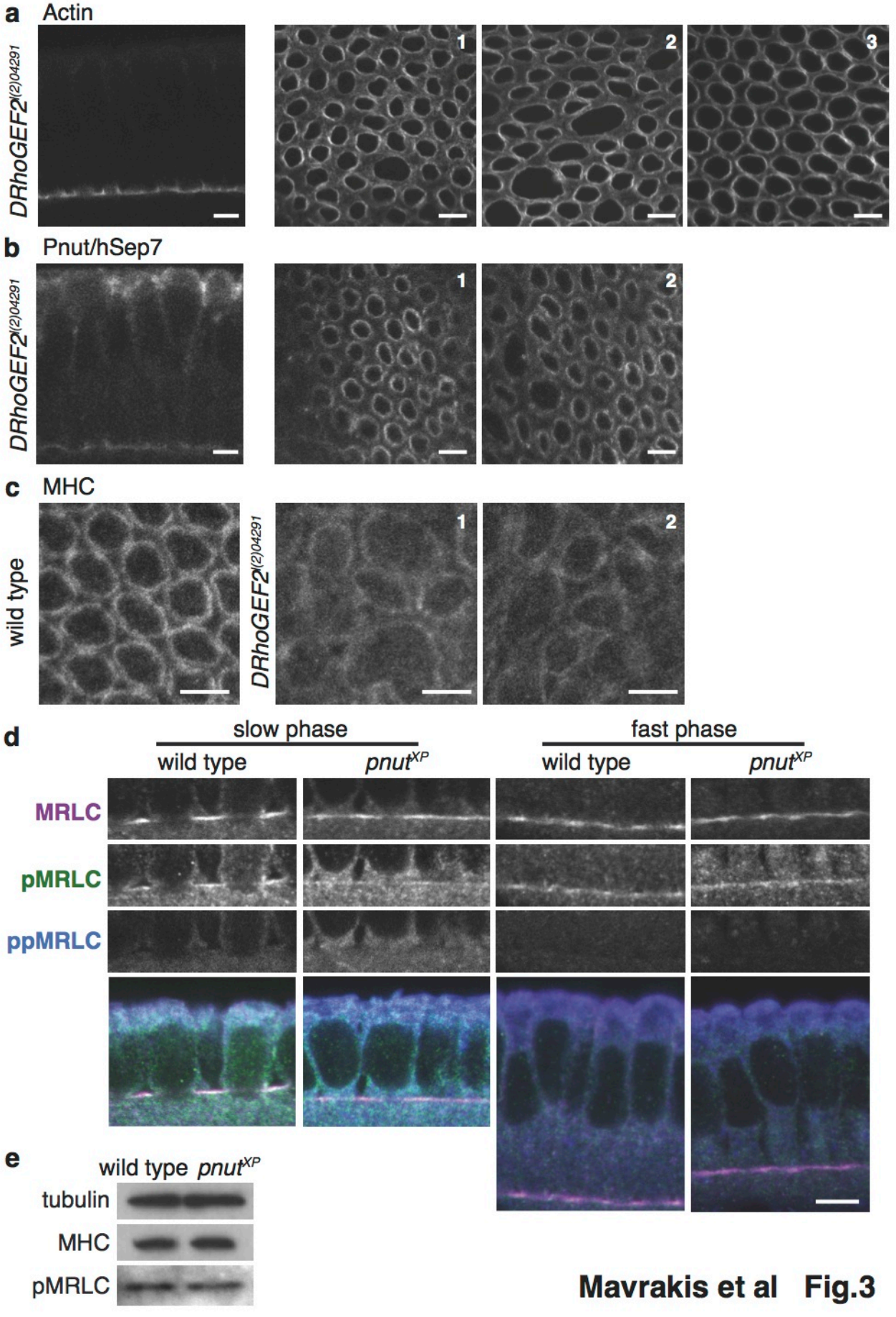

Mavrakis et al Fig.3

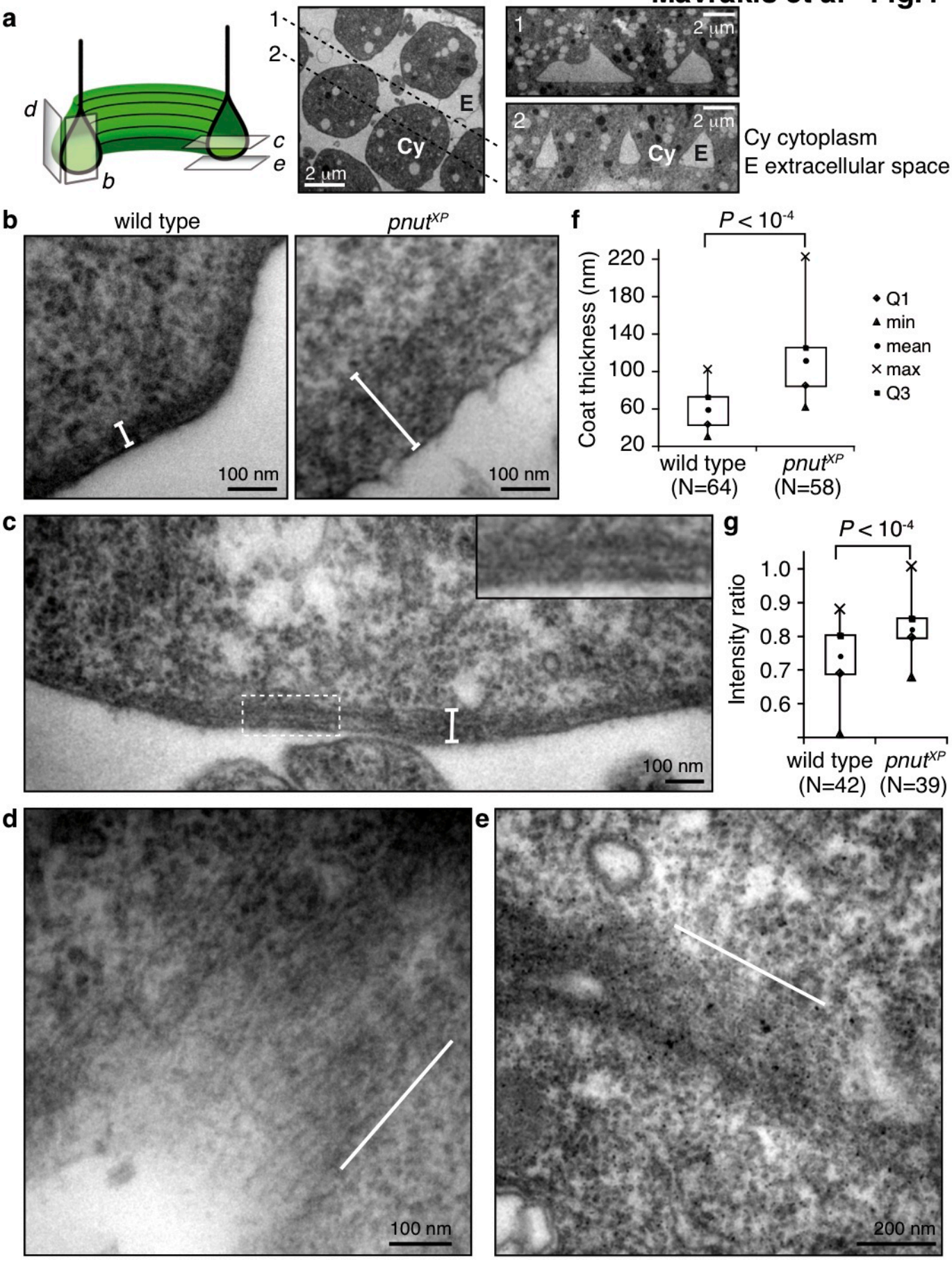
a
d
b
c
e
1
2
E
Cy
2 μm
Cy cytoplasm
E extracellular space
b
wild type
pnutXP
100 nm
f
P < 10-4
Coat thickness (nm)
220
180
140
100
60
20
wild type
(N=64)
pnutXP
(N=58)
Q1
min
mean
max
Q3
c
g
P < 10-4
Intensity ratio
1.0
0.9
0.8
0.7
0.6
wild type
(N=42)
pnutXP
(N=39)
d
e
200 nm

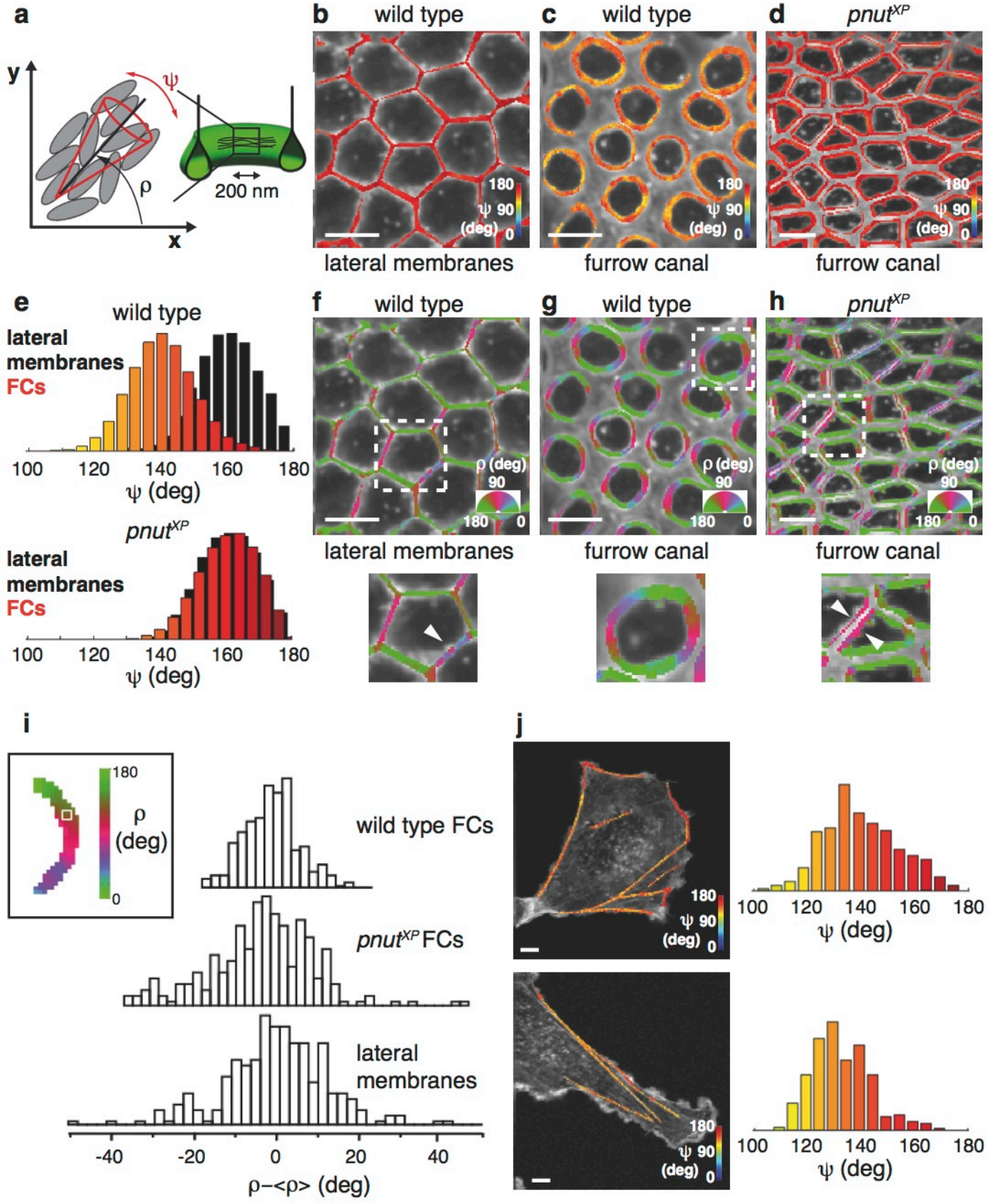

Mavrakis et al Fig.5

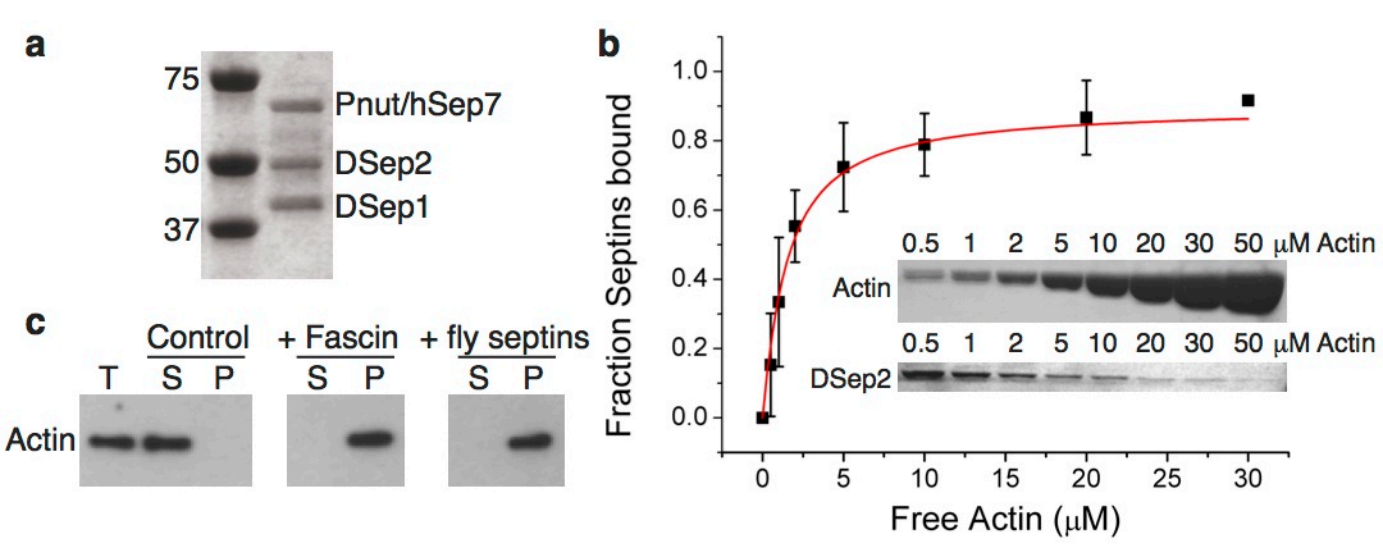

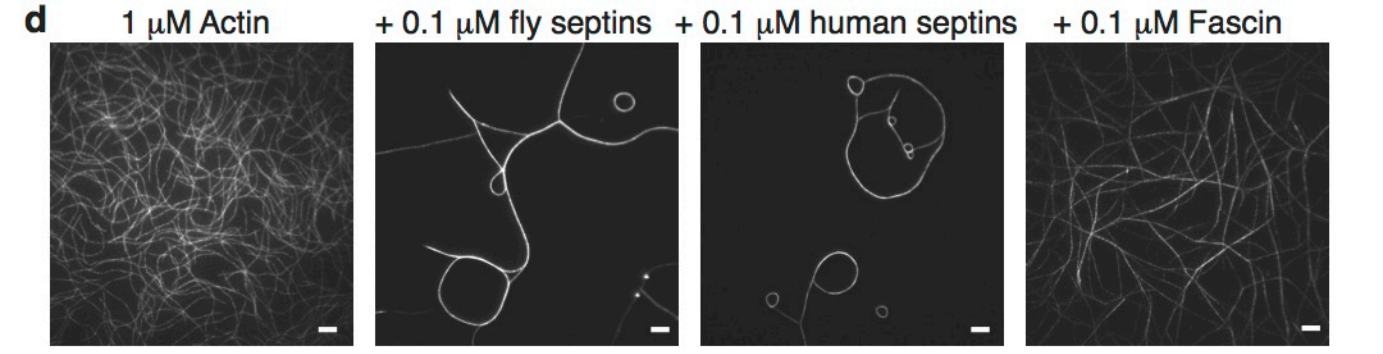

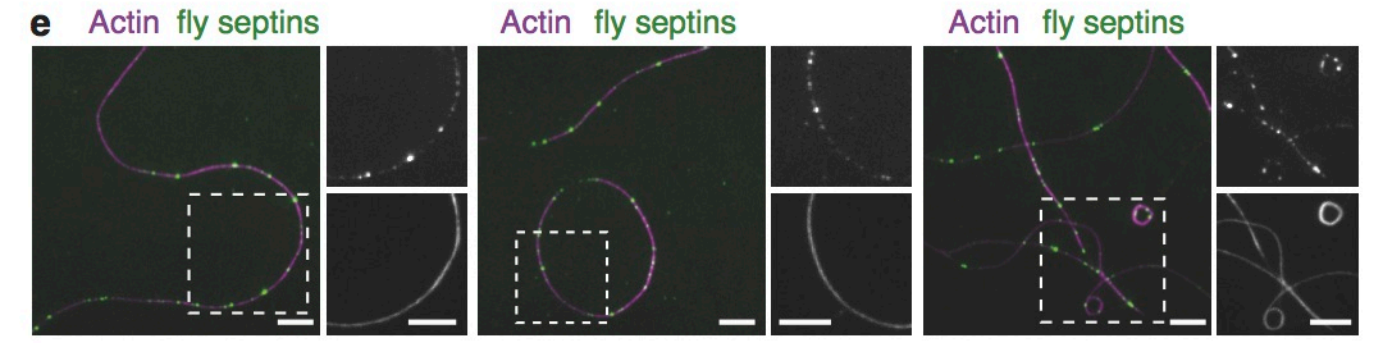

Mavrakis et al Fig.6

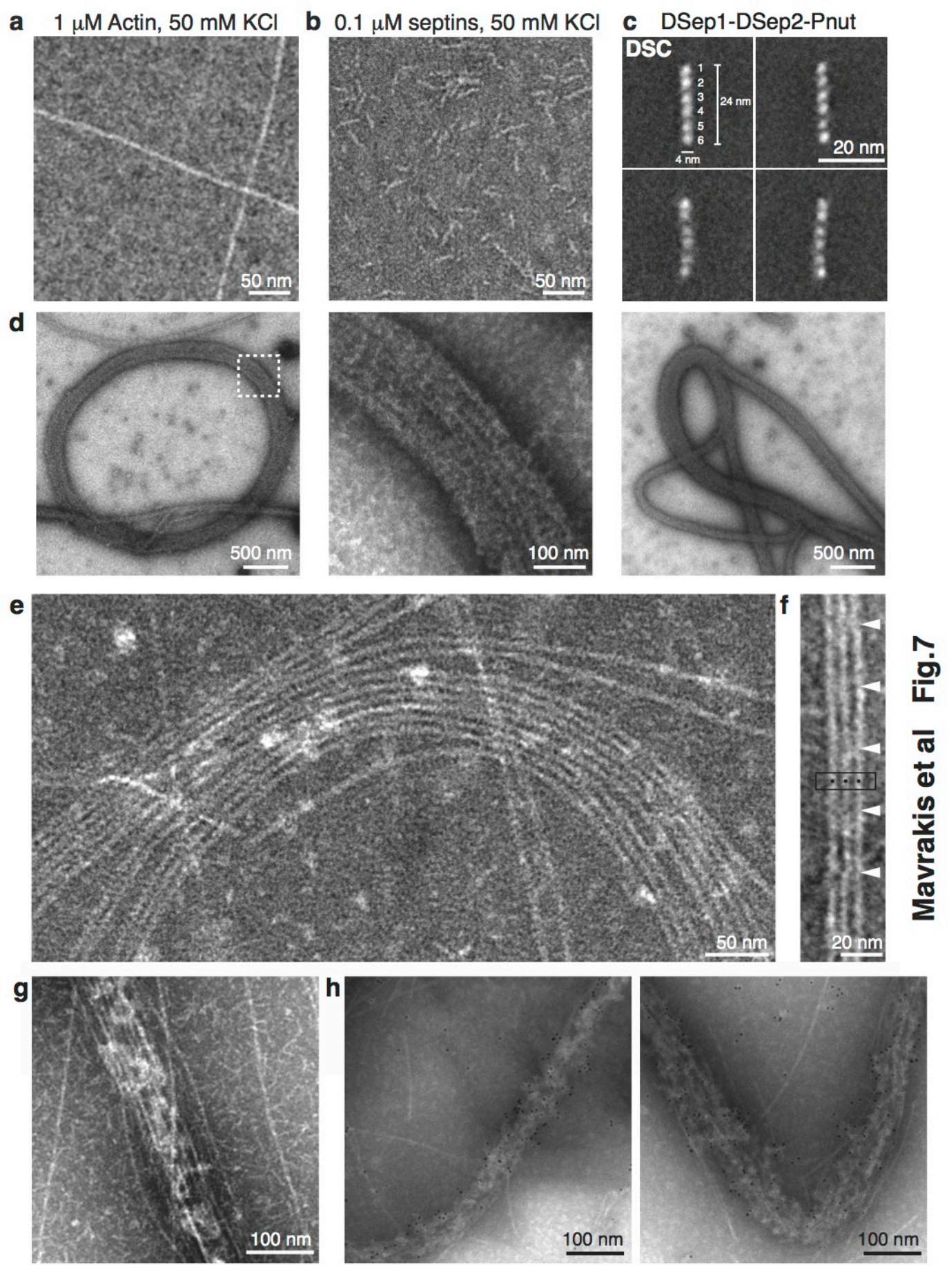
a
1 μM Actin, 50 mM KCl
50 nm
b
0.1 μM septins, 50 mM KCl
50 nm
c
DSep1-DSep2-Pnut
DSC
1
2
3
4
5
6
24 nm
4 nm
20 nm
d
500 nm
100 nm
500 nm
e
50 nm
f
20 nm
g
100 nm
h
100 nm
100 nm
Mavrakis et al Fig.7

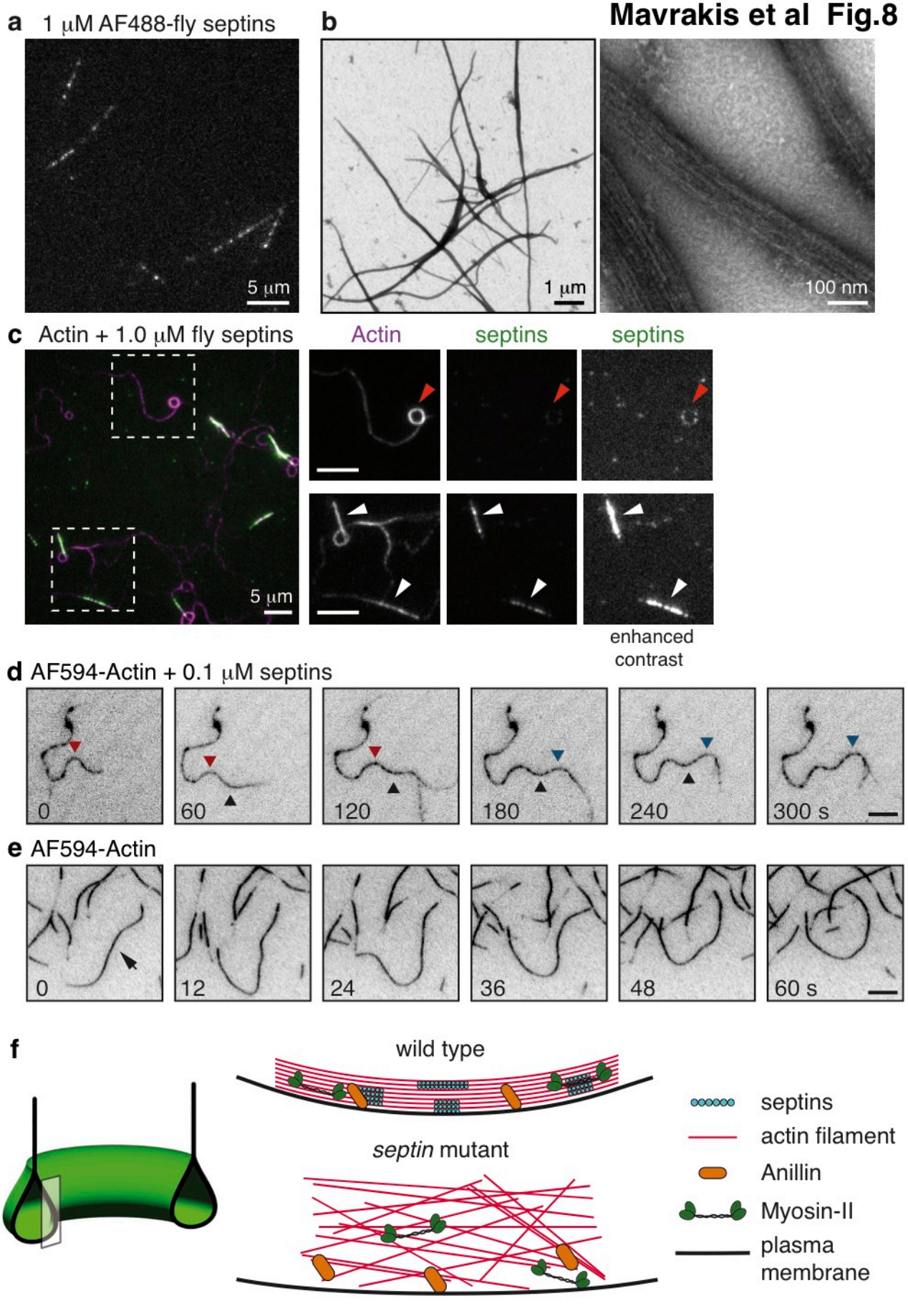
a
1 μM AF488-fly septins
5 μm
b
1 μm
100 nm
c
Actin + 1.0 μM fly septins
5 μm
Actin
septins
septins
enhanced contrast
d
AF594-Actin + 0.1 μM septins
0
60
120
180
240
300 s
e
AF594-Actin
0
12
24
36
48
60 s
f
wild type
septin mutant
septins
actin filament
Anillin
Myosin-II
plasma membrane

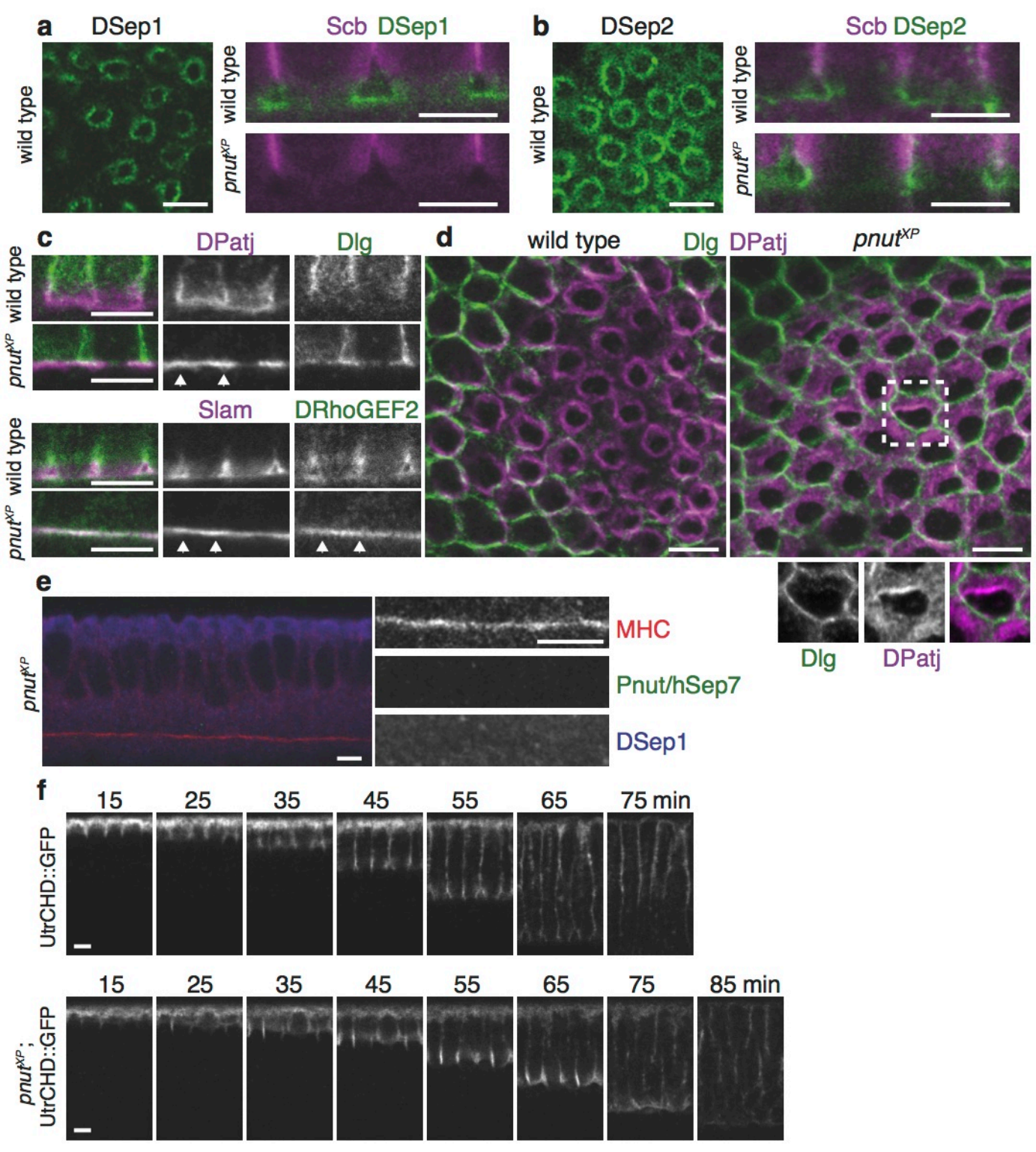

Mavrakis et al Sup.Fig.1

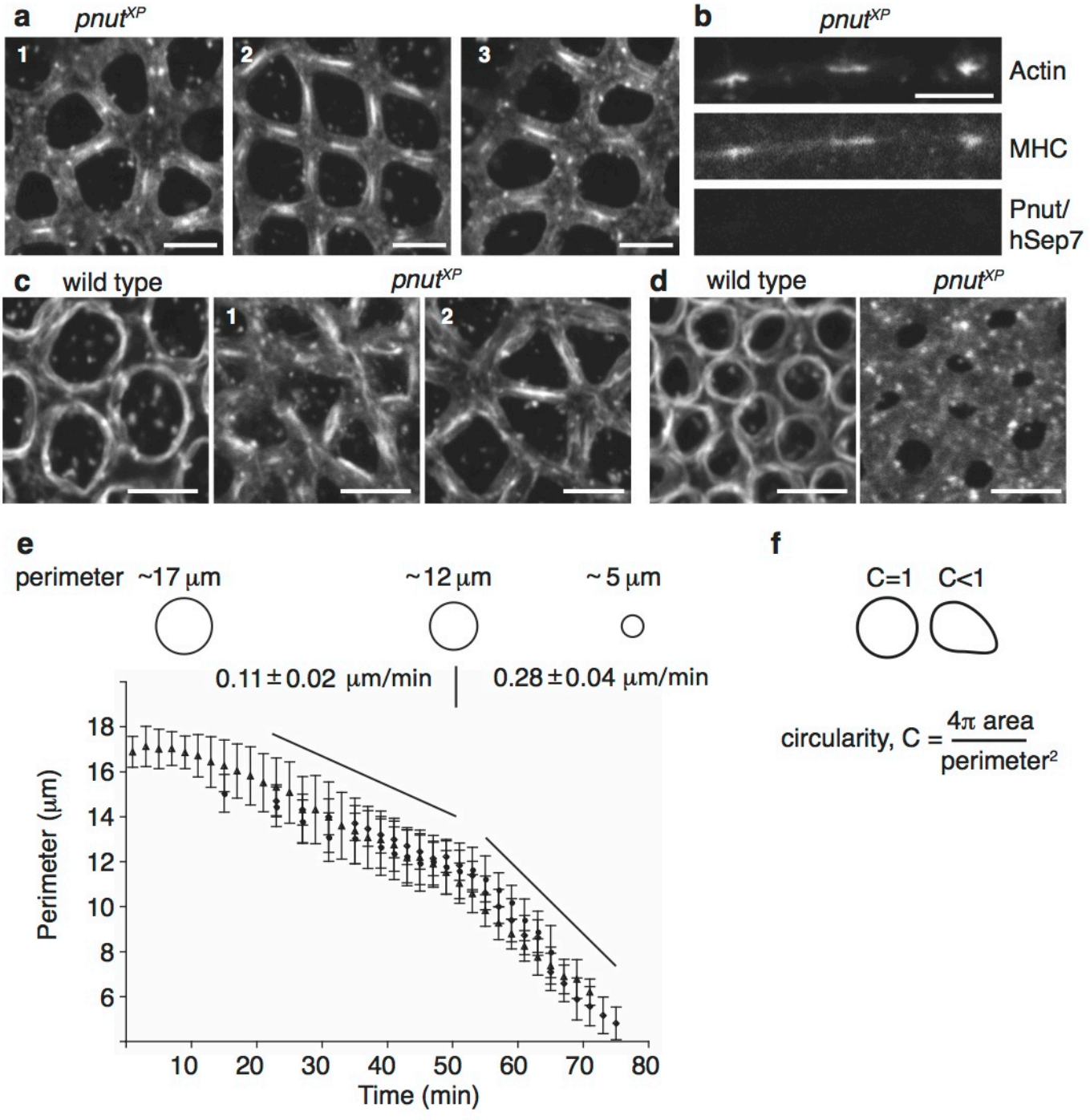

Mavrakis et al Sup.Fig.2

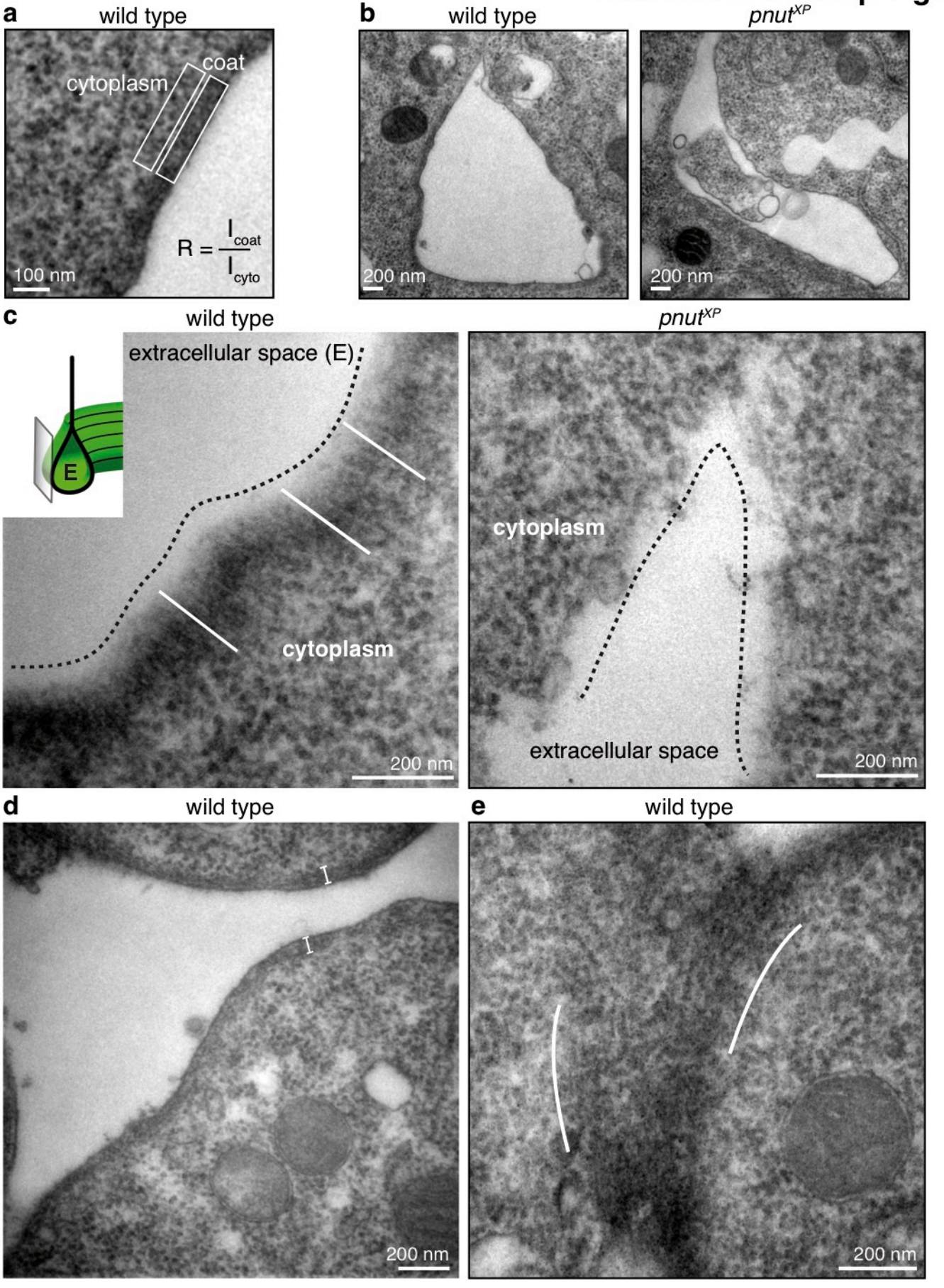
a
wild type
coat
cytoplasm
R = I coat / I cyto
100 nm
b
wild type
pnutXP
200 nm
200 nm
c
wild type
pnutXP
extracellular space (E)
E
cytoplasm
200 nm
cytoplasm
extracellular space
200 nm
d
wild type
200 nm
e
wild type
200 nm

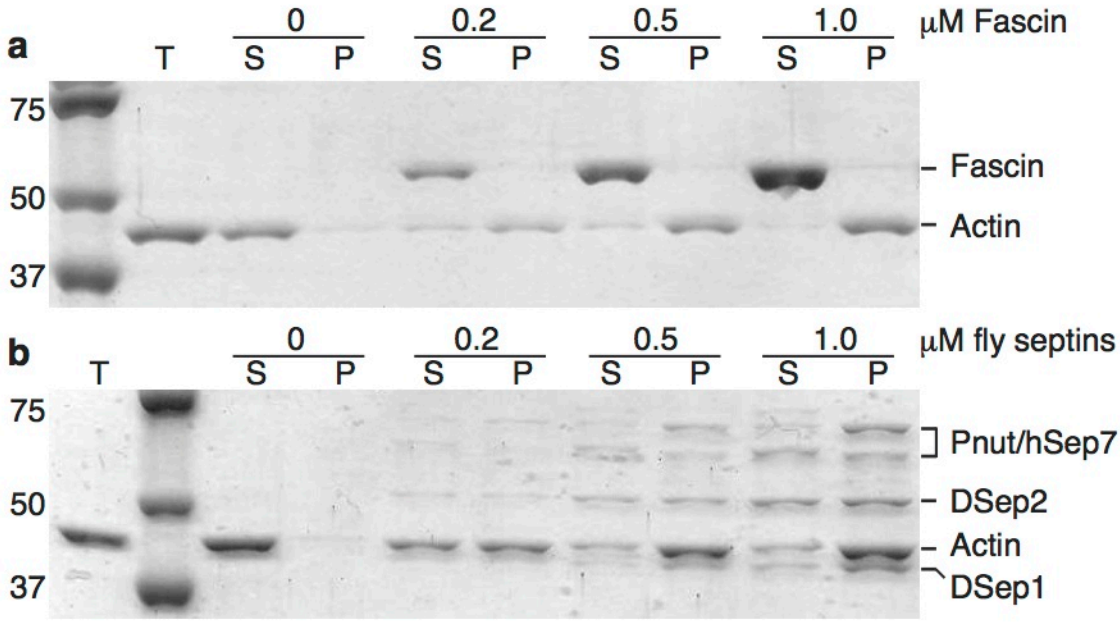

Mavrakis et al Sup.Fig.4

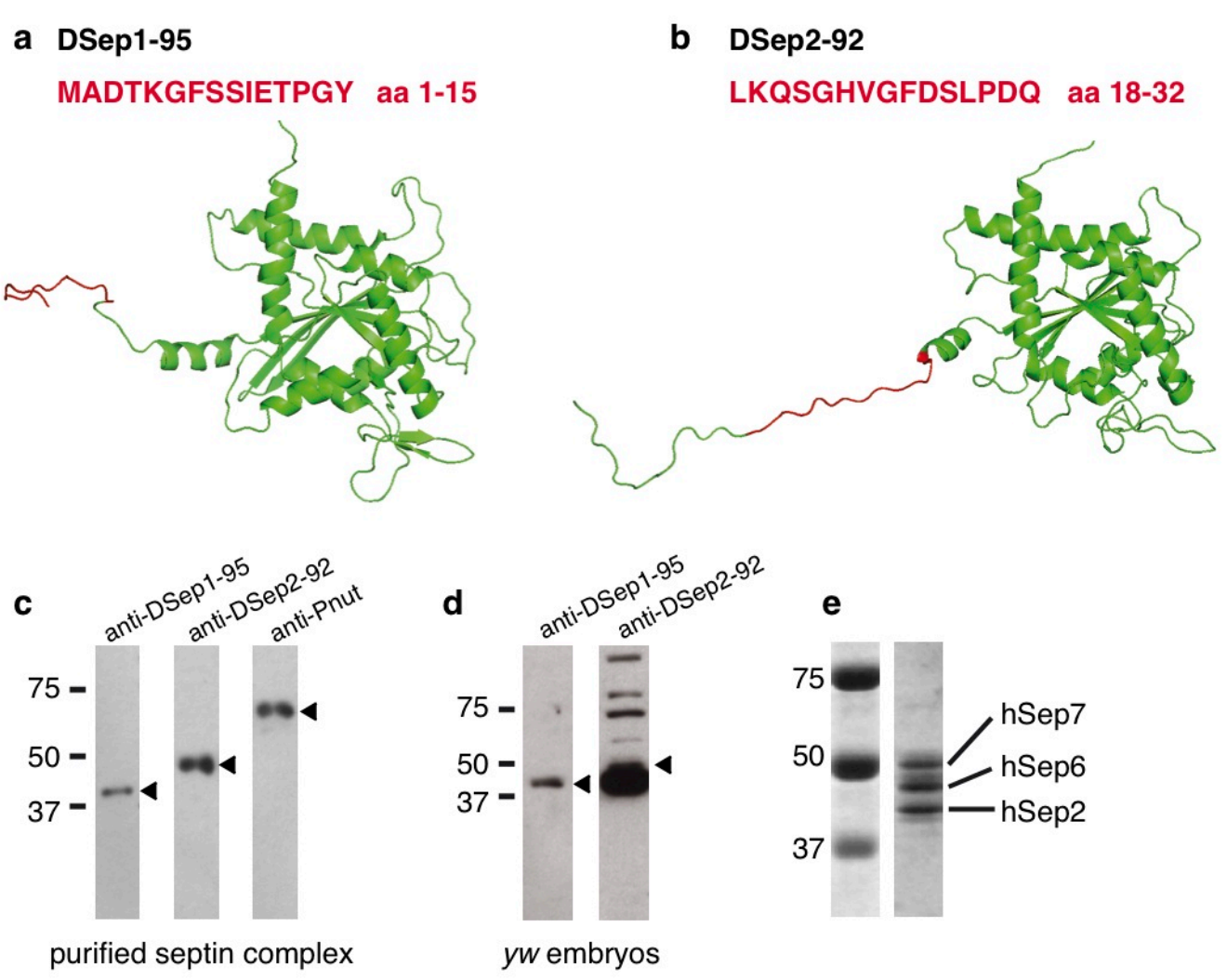

Mavrakis et al Sup.Fig.5